Sea ice concentration satellite retrievals influenced by surface changes due to warm air intrusions: A case study from the MOSAiC expedition

Janna E. Rückert[1,2,*], Philip Rostosky[1,2], Marcus Huntemann[2], David Clemens-Sewall[3], Kerstin Ebell[4], Lars Kaleschke[5], Juha Lemmetyinen[6], Amy R. Macfarlane[7], Reza Naderpour[8], Julienne Stroeve[9,10,11], Andreas Walbröl[4], Gunnar Spreen[2]

[1]These authors contributed equally to this work.
[2]Institute of Environmental Physics, University of Bremen, Bremen, Germany
[3]Thayer School of Engineering, Dartmouth College, Hanover, USA
[4]Institute for Geophysics and Meteorology, University of Cologne, Cologne, Germany
[5]Alfred-Wegener-Institut Helmholtz-Zentrum für Polar und Meeresforschung, Bremerhaven, Germany
[6]Space and Earth Observation Centre, Finnish Meteorological Institute, Helsinki, Finland
[7]Institute for Snow and Avalanche Research SLF, Davos, Switzerland
[8]Eidg. Forschungsanstalt für Wald, Schnee und Landschaft WSL, Birmensdorf, Switzerland
[9]University of Manitoba, Winnipeg, Canada
[10]University College London, London, UK
[11]National Snow and Ice Data Center, USA
[*]janna.rueckert@uni-bremen.de

Abstract

Warm air intrusions over Arctic sea ice can rapidly change the snow and ice surface conditions and can alter sea ice concentration (SIC) estimates derived from satellite-based microwave radiometry without altering the true SIC. Here we focus on two warm moist air intrusions that produced surface glazing during the Multidisciplinary drifting Observatory for the Study of Arctic Climate (MOSAiC) expedition that reached the research vessel *Polarstern* in mid-April 2020. After the events, we observe increased SIC deviations between different satellite products, including climate data records, and especially an underestimation of SIC for algorithms based on polarization difference. To examine the causes of this underestimation, we use the extensive MOSAiC snow and ice measurements to

computationally model the brightness temperatures of the surface on a local scale. We further investigate the brightness temperatures observed by ground-based radiometers at frequencies 6.9 GHz, 19 GHz and 89 GHz.

We show that the drop in the retrieved sea ice concentration of some satellite products can be attributed to large-scale surface glazing, i. e., the formation of a thin ice crust at the top of the snowpack, caused by the warming events. Another mechanism affecting satellite products which are mainly based on gradient ratios of brightness temperatures, is the interplay of the changed temperature gradient in the snow and snow metamorphism. From the two analyzed climate data record products, one is less affected by the warming events. The low frequency channels at 6.9 GHz were less sensitive to these snow surface changes, which could be exploited in future retrievals of sea ice concentration.

1. Introduction

The frozen blanket of the Arctic Ocean, the Arctic sea ice, controls fluxes of heat, moisture and momentum between ocean and atmosphere. Arctic sea ice is also a habitat for marine organisms. As the Arctic is warming rapidly over the last decades, this integral component of the cryosphere is strongly affected, which has a multitude of consequences both locally and outside of the Arctic (Semmler et al., 2012; Fox-Kemper et al., 2021, e.g.,). During the last decades, the summer Arctic sea ice extent declined by about $-13\,\%$ (Perovich et al., 2017; Meier and Stroeve, 2022).

Observations from satellite microwave radiometers provide a more than 40-year-long time series of Arctic sea ice area (Spreen and Kern, 2017), giving main insights for sea ice research and providing findings for climate research (Meredith et al., 2019). Retrievals of sea ice concentration (i. e., the percentage of an area covered by sea ice) using passive microwave sensors take advantage of the strong microwave emission contrast of ice and ocean, i.e., high for ice and often several tens of Kelvin lower for ocean. Retrieval algorithms are either (i) based on polarization difference, (ii) combine different frequencies, or (iii) use both, different polarizations and frequencies. Overviews and inter-comparisons of different retrieval algorithms are for example given in Ivanova et al. (2015) and Andersen et al. (2006, 2007). In this case study, involving two moist and warm air intrusions in April 2020, we investigate the performance of common sea ice concentration retrievals of type (i) and (iii).

Moist air intrusions transporting water vapor poleward play an important role in the Arctic climate system. They increase the downward longwave radiation flux and the skin temperature and thus contribute to Arctic warming in winter (Woods et al., 2013; Hao et al., 2019). There is evidence for an increase in the frequency of extreme warming events, atmospheric rivers and cyclones in the central Arctic in winter, related to an increase in meridional heat and moisture transport (Graham et al., 2017; Valkonen et al., 2021; Rinke et al., 2017; Hao et al., 2019; Henderson et al., 2021; Woods and Caballero, 2016; Zhang et al., 2023). We will refer to these events as "warm air intrusions" in the following acknowledging that for specific events they can be different, e. g., in terms of moisture. Warm air intrusions and associated wind and temperature changes can alter the sea ice concentration by ice advection, breaking the ice and opening leads, or, to a lesser degree, by melting the ice (mainly in connection with upwelling of warmer, e. g., Atlantic, water along the ice margins but also by direct melting of the ice surface). However, warm air intrusions can also significantly change the atmosphere and the surface in ways that alter satellite-measured microwave brightness temperatures (TB) without changing the ice concentration (Liu and Curry, 2003). These changes can cause spurious changes in sea ice concentration products (Tonboe et al., 2003) based on brightness temperatures, i. e., they can cause wrong ice concentration retrievals in some cases. One possible effect on the snow surface is surface glazing. By glazing we mean the formation of a thin ice layer on top of the snow due to melt or precipitation (rain on snow (Stroeve et al., 2022, e.g.)) or other mechanisms, e. g. winds, as observed for example in Antarctica (Scambos et al., 2012). Onstott et al. (1987) found that a crust reduces emissivity at 37 and 94 GHz significantly because of scattering within this layer. Smith (1996) and Comiso et al. (1997) conjectured that ice layers in the snow can be a reason for an underestimation of ice concentration referring to Mätzler et al. (1984). Mätzler et al. (1984) showed that ice layers introduce interfaces with different refractive indices, effecting especially the horizontally-polarized brightness temperatures close to the Brewster angle as described by the Fresnel equations and therefore alter the polarization difference. Rees et al. (2010) also observed this effect due to ice lenses on snow on land in the Arctic.

To study and increase the understanding of the various processes that lead to the strong recent changes in the Arctic climate, the Multidisciplinary drifting Observatory for the Study of Arctic Climate (MOSAiC) (Nicolaus et al., 2022; Shupe et al., 2022a; Rabe et al., 2022) expedition was conducted for a full year from October 2019 to September 2020. The research icebreaker *R/V Polarstern* (Alfred-Wegener-Institut Helmholtz-Zentrum für Polar- und Meeresforschung, 2017) was moored to a sea ice floe and drifted with it. During the campaign ship-based, ground-based, and airborne measurements of the ocean, sea ice, atmosphere, biogeochemistry and ecosystem in the vicinity of the ship were collected. The area within about 2 km of *Polarstern* — named the 'Central Observatory' (CO)— was intensively studied.

Warm air intrusions in April 2020

After a long period of cold winter conditions, two warm and moist air intrusions in April 2020 dramatically warmed the CO (Shupe et al., 2022b). During the warm air intrusions, air temperatures increased by up to 30 °C at the MOSAiC site, getting close to and even above the melting point. The atmospheric events included record-breaking total water vapor (Rinke et al., 2021) and high liquid water path, increased wind speeds, precipitation, as well as changes in the aerosol regime (Dada et al., 2022) and surface snow metamorphism. Before, during, and after the warm air intrusion the actual SIC in the vicinity of MOSAiC was high ($> 95\,\%$). Single leads opened during the events but nothing major in comparison to the periods before and after. This is confirmed by optical (MODIS) and radar (Sentinel-1) satellite data as well as by observations from the expedition participants and by helicopter-borne thermal infrared imagery (Thielke et al., 2022). The latter gives a value for lead fraction, i. e., fraction of open water and thin ($< 30\,$cm) young ice, of the order of $1.5\,\%$ over the Central Observatory on April 23. Still the warm air intrusion events affected satellite products of SIC. In conjunction with the warming events, most satellite products showed a (wrong) decrease in SIC and inter-product variability increased.

Microwave emission from open water depends mainly on surface temperature and surface roughness related to wave and foam formation. The microwave emission of the snow-ice system, on the other hand, depends on snow and sea ice properties such as density, temperature, salinity, stratification and microstructure. Warm air intrusions can strongly impact these parameters and can thus change the emission of the snow-ice system. Therefore, in order to understand their impact on the sea ice concentration retrievals, we analyze the detailed snow and ice observations taken during MOSAiC (Nicolaus et al., 2022) and simulate the impact of the April warm air intrusions on the microwave emission of the sea ice. This is done on a floe-wide scale.

We then 'zoom in' further to adopt a local perspective and investigate the ground-based radiometer observations taken at the Remote Sensing Site during MOSAiC.

Of particular interest on all scales are responses of brightness temperatures to large-scale surface glazing, which was observed at the MOSAiC CO.

In this paper, we study differences between several satellite ice concentration products related to the April 2020 warm air intrusions. To explain the differences, we investigate the effect of these events on microwave brightness temperatures. We present the suite of such observations at *Polarstern* by satellite and ground-based radiometers on the ice floe measuring at the same frequencies (6.9 GHz, 19 GHz and 89 GHz). We use in-situ snow and ice observations and microwave emission modelling to explore the impacts of glazing and snow metamorphism on brightness temperatures and, consequently, on SIC retrievals. The results are structured by the different scales that we are observing at, from a satellite view (Section 3.1) via a floe-wide perspective (Section 3.3) to a specific on-ice site (Section 3.4).

2. Data

2.1. Sea ice concentration: satellite products

We compare the sea ice concentration (SIC) around *Polarstern* based on different algorithms developed for satellite passive microwave remote sensing using different frequencies and polarization combinations. The datasets used are described in more detail in the following subsections. Table 1 provides an overview including the frequency channels that are used to compute SIC and the grid spacing. All products are available daily. The collocation procedure is the same for all products: In order to account for drift we use *Polarstern's* position resampled to hourly values and then choose the closest grid point in the satellite product for each hour. We then average over the whole day.

2.1.1. ASI Sea Ice algorithm

The ASI algorithm exploits the high spatial resolution of near 90 GHz channels and was initially developed for SSM/I sensors (Svendsen et al., 1987; Kaleschke et al., 2001). It was later adapted for the AMSR-E and AMSR2 sensors (Spreen et al., 2008; Melsheimer, 2019). The polarization difference (PD)

$$\mathrm{PD} = \mathrm{TB\,V} - \mathrm{TB\,H}, \tag{1}$$

where V denotes vertical and H horizontal polarization, at 89 GHz over open ocean is larger than over sea ice. This is used by the algorithm to distinguish between these two surface types. The sea ice concentration is retrieved by a third-order polynomial of PD where the coefficients are determined by the tie points, i. e., typical values of PD over water ($P0$) and consolidated ice, i. e., 100 % ice concentration ($P1$). To correct for weather influences over open ocean, weather filters are applied. Here, we use the dataset operationally available on a 6.25 km grid at `https://seaice.uni-bremen.de` and `https://meereisportal.de`.

2.1.2. NASA Team Algorithm

The NASA Team algorithm (Cavalieri et al., 1984, 1997) uses vertically and horizontally-polarized brightness temperature channels to calculate the polarization ratio, $PR = \mathrm{PD}/(\mathrm{TB\,V} + \mathrm{TB\,H})$, of 19.35 GHz, called PR(19) in the following, and the spectral gradient ratio $GR = (\mathrm{TB\,37V} - \mathrm{TB\,19V})/(\mathrm{TB\,37V} + \mathrm{TB\,19V})$ between TB 19.35V and TB 37V, called GR(37/19) in the following. These two ratios are then compared in a scatter plot where they form clusters. These clusters can be identified as being correspondent to three surface types (first-year ice, multiyear ice and ice-free ocean) and for each type three constant tie points are determined (for each frequency channel). Values between the tie points then represent mixtures of surface types. Weather filters are applied additionally. We use the NASA TEAM SIC operational product provided as part of the NOAA/NSIDC Climate Data Record of Passive Microwave Sea Ice Concentration, Version 4 (Meier et al., 2021).

2.1.3. NSIDC Climate Data Record

The National Snow and Ice Data Center (NSIDC) provides sea ice concentration estimates as a Climate Data Record (CDR) starting in 1978 (Meier et al., 2021). Here, SIC is computed both by NASA Team (see above) and the NASA Bootstrap algorithm (Comiso, 1986; Comiso et al., 2017). The Bootstrap algorithm is based on relationships of TB combinations of 19V and 37V, and 37V and 37H. Clusters of pure surface types are determined in brightness temperature scatter plots of these combinations. Tie points are derived daily based on these clusters. Additionally, weather filters are applied. Then, the higher concentration value from the two algorithms is chosen for each grid cell. We use the NSIDC CDR operational product provided by the NOAA/NSIDC Climate Data Record of Passive Microwave Sea Ice Concentration, Version 4 (Meier et al., 2021).

2.1.4. OSI SAF Climate Data Record

OSI SAF Global Sea Ice Concentration interim climate data record (OSI-SAF iCDR), release 2, provides daily sea ice concentration, starting in 2016 and using data from the SSMIS sensors from NOAA CLASS (EUMETSAT Ocean and Sea Ice Satellite Application Facility., 2017). This sea ice concentration data set, OSI-430-b, is based on a dynamic algorithm (Lavergne et al., 2016, 2019), gener-

Table 1: Summary of sea ice concentration products used.

Algorithm	Frequencies	Grid spacing
ASI	PD 89	6.25 km
NSIDC NASA Team	19.35V, 19.35H, 37V	25 km
NSIDC CDR	19.35V, 19.35H, 37V, 37H	25 km
OSI-SAF iCDR	19.35V, 37V, 37H	25 km

alizing the Bristol algorithm (Smith, 1996). Brightness temperatures at 19V, 37V and 37H span a 3-D space. Within this space, clusters or shapes close to lines for closed-ice and water are existent. The algorithm then projects the brightness temperature data on an optimized plane. This projection is found using daily updated training data sets, one for fully ice-covered and one for open water areas. The unit vector of this plane is found by principal component analysis (direction of highest variance in ice concentration) and is then rotated to maximize accuracy. The final sea ice concentration is then calculated by a weighted linear combination of SIC computed from an algorithm dynamically tuned to perform better over open water and one dynamically tuned to perform better over high-concentration ice conditions, both applied in the respectively optimized planes in TB space. Additionally, the TBs are corrected using operational analysis and forecast data from the European Centre for Medium-range Weather Forecasts (ECMWF) to account for atmospheric influences.

2.2. Satellite remote sensing

We investigate brightness temperatures measured by the microwave scanning radiometer AMSR2 on the GCOM-W1 spacecraft from the Japan Aerospace Exploration Agency (JAXA), launched May 18, 2012. AMSR2 orbits the Earth at an altitude of 700 km in a near-polar, sun-synchronous sub-recurrent orbit with a swath width of 1450 km. The dual-polarized sensor has instantaneous fields of view (IFOV) ranging from 62 km$\times$35 km at 6.9 GHz to 5 km $\times$ 3 km at 89 GHz. We use the swath data, both ascending and descending, of the Level 1R product matched to the resolution of 6.9 GHz (Maeda et al., 2016), corresponding to an IFOV of 62 km$\times$35 km. This product matches antenna patterns so that the brightness temperatures for all frequencies have the same field of view, facilitating easier comparisons between different frequencies. For every overflight of *Polarstern* we chose the measurement closest to the vessel's hourly position. There are between five and seven overflights per day. For clarity, we show daily averaged values of brightness temperatures at 6.9 GHz, 18.7 GHz, 36.5 GHz and 89 GHz in Figure 4.

2.3. Ground-based remote sensing

We focus on two microwave radiometers deployed during MOSAiC observing the surface at frequencies ranging from 6.9 GHz to 89 GHz, similar to AMSR2. Details are provided in the supplement Section 6.4. It is to note that due to increased snow accumulation in front of the instruments after the warm air intrusions, the snow was much deeper around the ground-based radiometers compared to the surrounding MOSAiC floe. Especially during and after the second warm air intrusion, deep snow drifts formed in the field of view (FoV) of some radiometers (see supplemental Section 6.4).

2.4. Snow data

Detailed snow measurements were performed during MOSAiC. In this study, we analyze 132 SnowMicroPen (SMP) profiles (Macfarlane et al., 2021) taken between April 08 and April 27 to support our interpretation of the observed satellite signals. From the raw SMP observations (penetration resistance) snow density and specific surface area (SSA) can be estimated using empirical models (Proksch et al., 2015; King et al., 2020). From density and SSA, the exponential correlation length can be estimated, a parameter describing the microstructure of the snow which is used in common snow microwave emission models (Tonboe et al., 2006, e.g.,).

2.5. Supporting data

2.5.1. Met Tower temperature

We use the 2 m air temperature recorded from the 10 m meteorological mast installed on the floe (Cox et al., 2021).

2.5.2. Precipitation

To illustrate the timing of precipitation, we use data from the *Vaisala* Present Weather Detector 22 (PWD22) precipitation gauge, an optical device that was installed on the deck of *Polarstern* and operated by the US Department of Energy Atmospheric Radiation Measurement (ARM) program (Shi, 2019). Here, we use 1 minute mean precipitation rates (Figure 3). This product was also used as reference product in an inter-comparison of different snow precipitation sensors by Wagner et al. (2022).

2.5.3. Total water vapor from radiosondes

The Level 2 dataset of balloon-borne radiosondes from the MOSAiC expedition (Maturilli et al., 2021) was used to calculate total water vapor (TWV) from the measured temperature, pressure and relative humidity profiles from the *Polarstern* helicopter deck (at about 10 m height) to about 30 km altitude using the formula for vapor pressure over liquid water below 0°C by Hyland and Wexler (1983) as done in Walbröl et al. (2022). During the warm air intrusions, the radiosondes were launched more often, up to seven times a day, while during the other periods they were launched four times a day.

2.5.4. Liquid water path from HATPRO radiometer

We use liquid water path (LWP) retrieved from the ground-based low frequency HATPRO (Humidity and Temperature Profiler) microwave radiometer operated onboard the research vessel *Polarstern* during MOSAiC as input parameter to model the atmosphere. The retrieved LWP is based on the retrieval algorithm as described in Nomokonova et al. (2019). The radiometer has a temporal resolution of 1 second. More information on this data can be found in Walbröl et al. (2022).

2.5.5. Reanalysis ERA5

From ECMWF fifth generation reanalysis ERA5 (Hersbach et al., 2020) we use long- and shortwave radiation from the grid cell closest to *Polarstern* for the SNOWPACK model simulations (Section 2.4).

2.5.6. Terrestrial laser scanner TLS

Supporting information about the snow surface topography was derived from terrestrial laser scan (TLS) data taken on April 17 and on April 22 (Clemens-Sewall et al., 2022c). The TLS uses a scanning, 1550 nm laser, to generate a three-dimensional point cloud of the snow and ice surface at cm-scale resolution. See Deems et al. (2013) for a review of TLS applications to snow depth measurements. Wind-blown snow particles were filtered out of TLS data using the FlakeOut method (Clemens-Sewall et al., 2022a). From the measured topography and its changes, we can deduce the changing snow thicknesses and effective incidence angles (i.e., the incident angle of the tilted surface with respect to the radiometer) within the footprints of the radiometers. The TLS data also includes the backscatter reflectance of the surface at 1550 nm. Glazed areas are identifiable in this data, because surface glazing reduces the backscatter reflectance (glazing increases forward scattering and absorption).

3. Results

In the following we describe the temporal development of the retrieved sea ice concentration and satellite-measured microwave brightness temperatures, first on a large scale and then locally around *Polarstern*.

For the local analysis, we further describe the floe snow distribution by using the SMP measurements as model input to analyze the evolution of brightness temperatures. In a second step we change the perspective to an even smaller scale and study the data obtained by the ground-based radiometers. We then discuss the integration of the observations from the different scales. Finally, this allows us to come up with an interpretation of the satellite signal and the resulting differences in sea ice concentration estimates.

Figure 1 shows the temporal evolution of total water vapor from ERA5 over four days. The first intrusion, reaching the ship around April 16, originated in the Russian Arctic while the second one around April 19 was approaching from the North Atlantic. This illustrates the large area exposed to the warm air intrusions.

3.1. Satellite perspective: sea ice concentration and brightness temperatures

The two warm air intrusions were large scale events (Figure 1) and thus also visible at large scale in the satellite data. This becomes evident when looking at spatial maps of SIC (Figure 2). Here, we show the mean SIC for four consequent days prior and after the event. Note that the SIC from ASI (first row) has a much higher spatial resolution (6.25 km grid spacing compared to 25 km for all other products). The last column shows the difference between the two time periods. Blue colors denote a reduction of SIC after the events. In all products except for the NSIDC CDR, decreases of SIC are visible in the Central Arctic to different extents (black oval in the last column of Figure 2) as well as in the marginal ice zone. The strongest effect is observed for the ASI product, followed by NASA TEAM. Deviations between different products have increased after the events for all products. The reduction in SIC in the Central Arctic is larger than suggested by independent observations (from the ship and radar satellites) and likely caused by the warm air intrusions as will be discussed in the following.

MOSAiC measurements allow us to study the effect of these intrusions locally: total water vapor (TWV), liquid water path (LWP) and 2 m air temperature at *Polarstern* are shown in Figure 3, bottom row. For both warm air intrusions, the rising temperatures (up to the freezing point for the second) coincide with increased amounts of TWV (up to 13.4 mm) and LWP (up to around 0.47 mm). For

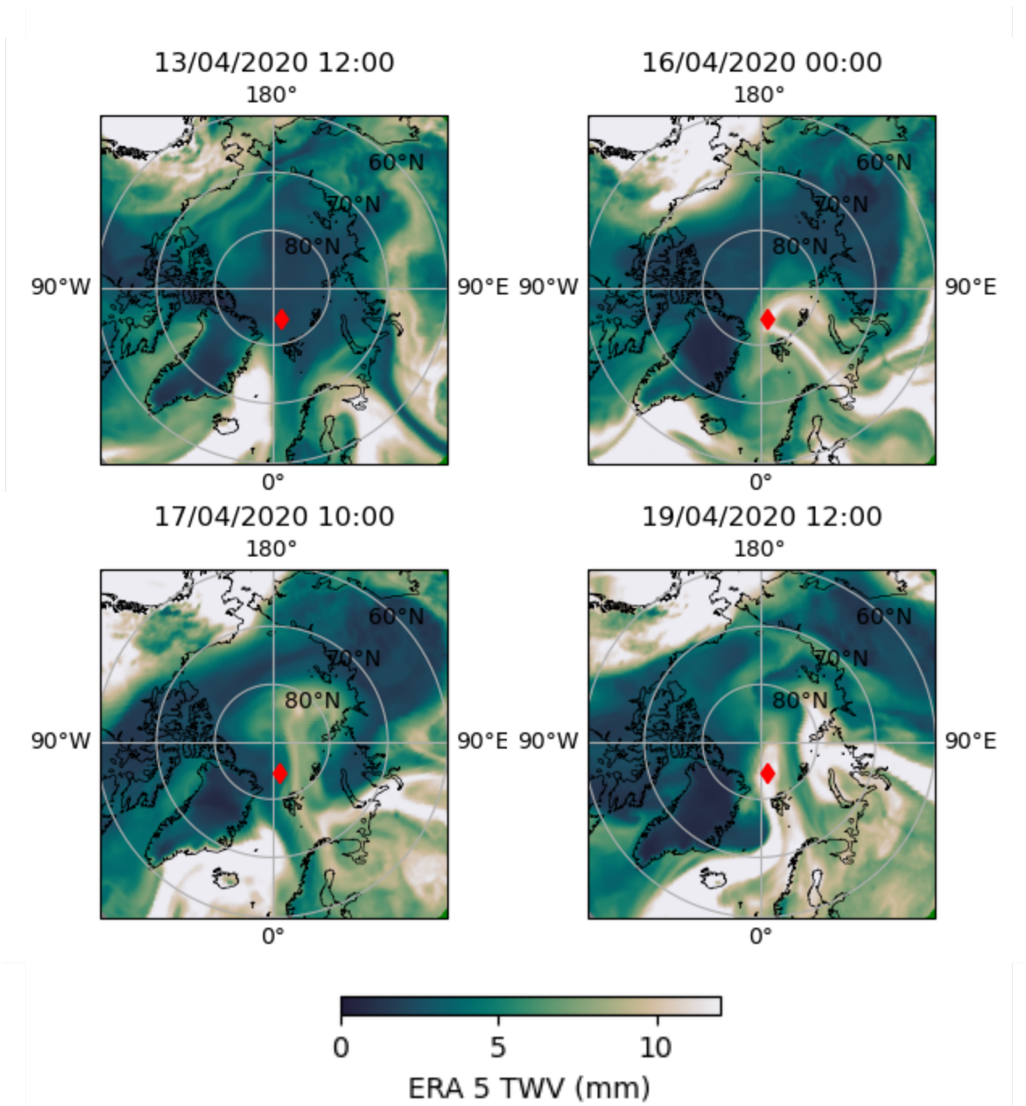

Figure 1: Total columnar water vapor (TWV, hourly values) from the reanalysis ERA5 for one day prior to the events and three days during the two warm air intrusions in April. The red diamond indicates the position of *Polarstern* at the day. The bright colors indicate high values of TWV.

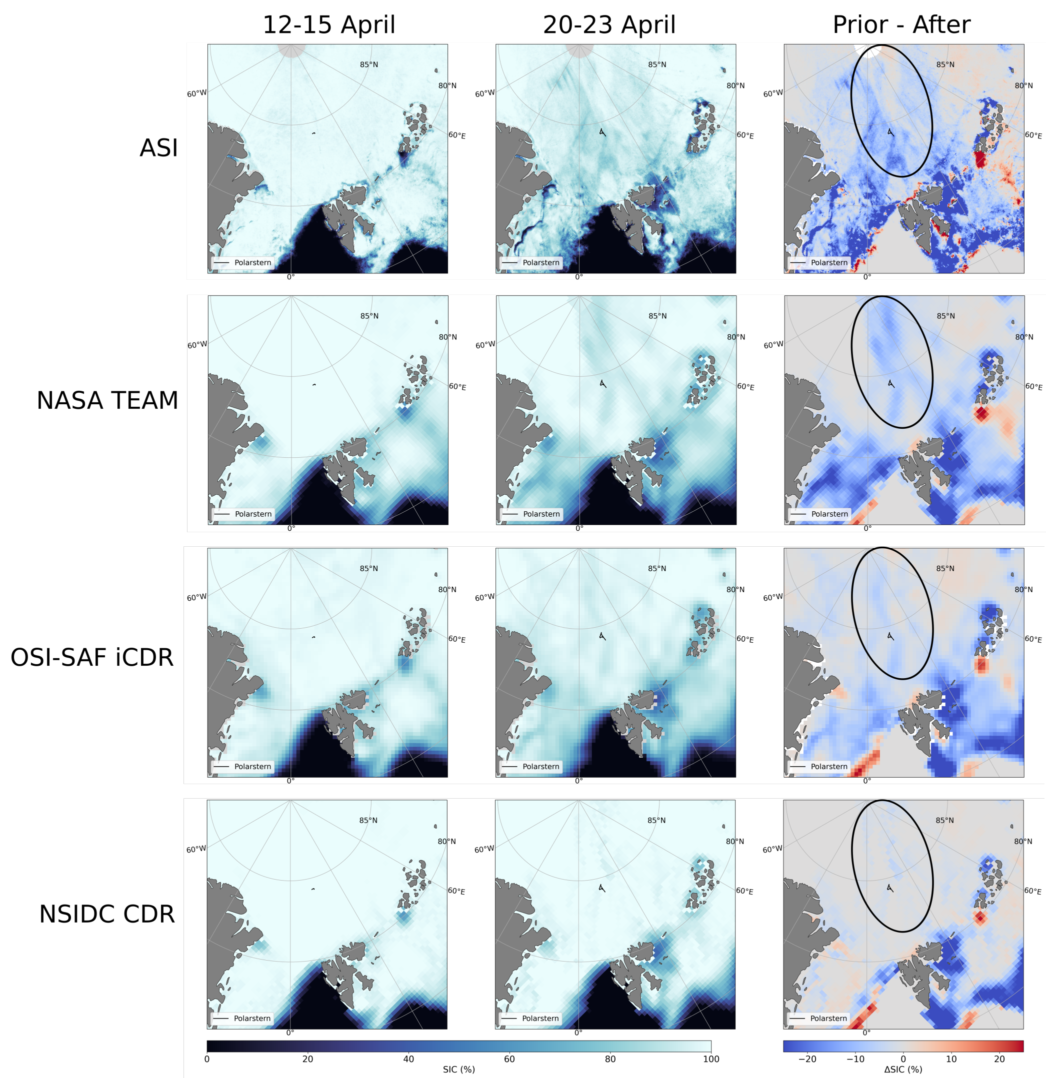

Figure 2: Sea ice concentration (SIC) from different satellite retrievals as four-day averages prior (first column) and after the intrusions (second column). The third column shows the difference between the second and first column, so the change in average SIC in the four days after the intrusions compared to the four days prior. The black oval in the last column marks a region where the different products deviate from each other after the events. *Polarstern's* drift track is shown by a black line.

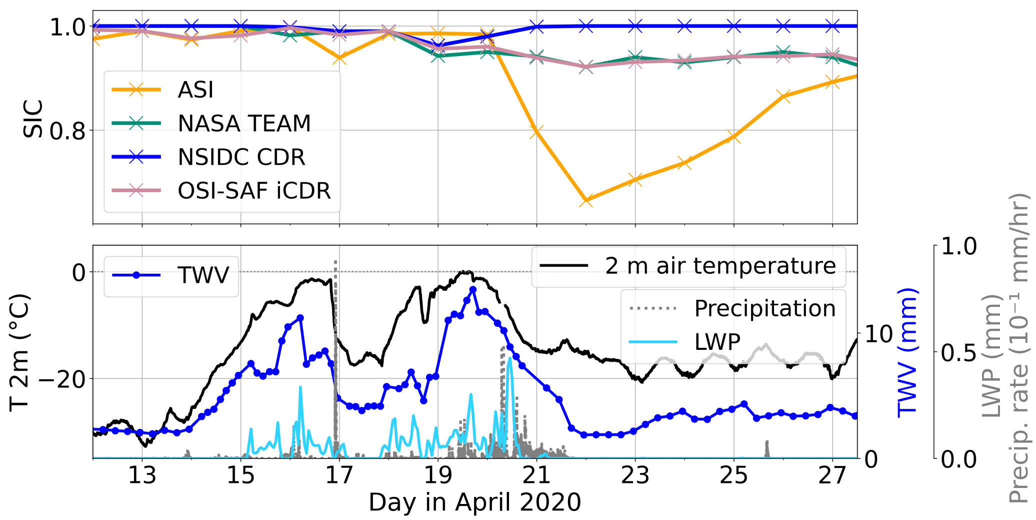

Figure 3: Sea ice concentration (SIC) and meteorological conditions during the events. Top row: SIC from four different operational products collocated to *Polarstern*. Bottom row: 2 m air temperature (black) from the Met Tower, total water vapor (TWV, dark blue) from radiosondes, liquid water path (LWP, light blue) from the HATPRO microwave radiometer (resampled to hourly values) and 1 min precipitation rates (grey) from the precipitation gauge (PWD22) installed on deck.

the ASI algorithm based on 89 GHz we observe a drop in SIC between the two warm air intrusions corresponding to the clear sky day on April 17 and a strong decline after the second event (Figure 3, top row). The SIC from NASA Team and OSI-SAF iCDR shows less variability during the intrusions but both decrease to 92 % on April 22 and do not recover thereafter. The NSIDC CDR, on the other hand, stays at 100 % SIC. This algorithm includes both NASA Team and the Bootstrap algorithm, see Section 2.1.3, with the latter compensating for the decrease observed in SIC from NASA Team as discussed later. Before the events, all algorithms showed high sea ice concentration around 100 %. Similar to the large scale view (Figure 2), the spread between different products increased after the events. Using the NSIDC CDR data as reference, we observe SIC differences of around 8 % for OSI-SAF iCDR and for NASA TEAM and up to 34 % for ASI. Although it has been observed by Tjernström et al. (2015) that warm air advections can cause rapid ice melt, and that dynamic effects can decrease SIC up to 3% in the high sea ice concentration domain. (Aue et al., 2022; Schreiber and Serreze, 2020) here

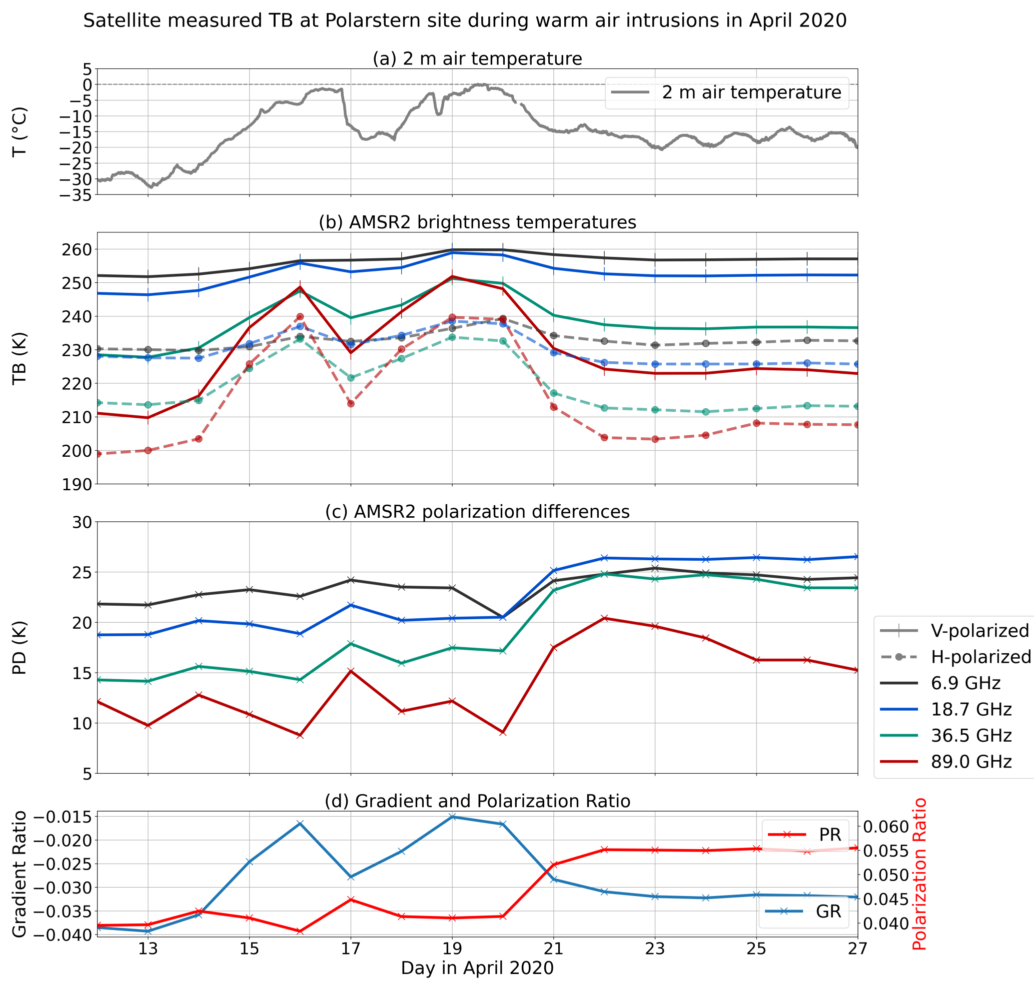

Figure 4: Effect of warm air intrusion on satellite-measured brightness temperatures. Top row shows the air temperature at 2 m (a). Collocated satellite measurement of TB (b) and PD (c) around *Polarstern* (daily averages). (d) Gradient ratio of 36.5 GHz and 18.7 GHz and polarization ratio of 18.7 GHz as defined in Section 2.1.2

the low sea ice concentration values at MOSAiC retrieved by some algorithms are underestimating the actual sea ice concentration.

In our field observations, we did not observe a dramatic decrease in ice concentration at this time. This is also confirmed by SIC derived from satellite thermal infrared data (MODIS instrument, only at clear sky, not shown), and such a significant drop in SIC can also not be seen in optical (MODIS) and radar (Sentinel-1) satellite data (not shown). To understand this underestimation of sea ice concentration, we analyze daily satellite AMSR2 brightness temperature data, shown in Figure 4 (b). The signature of the warming events is clearly visible in the brightness temperature time series at these frequencies. The higher frequencies (i. e., 36.5 GHz and 89 GHz) follow the air temperature evolution in Figure 4 (a) more closely. Especially ASI and NASA TEAM make use of polarization differences PD and polarisation ratios PR, respectively. All frequencies show an increased PD after the events as can be seen in the third row (c) of Figure 4. Again, the higher frequencies show a larger increase. The PD increase on April 22 compared to the mean of April 10 - April 13 ranges from a few Kelvin ($\approx$3 K) for 6.9 GHz up to around 9 K and 11 K for 89 GHz and 36.5 GHz, respectively. A smaller increase in PD at 89 GHz of a few Kelvin ($\approx$4 K) is already visible around April 17 between the two warm air intrusions. During that day, temperatures dropped and clear sky conditions connected with a high longwave radiation loss prevailed (Rinke et al., 2021). Images from the Panomax webcam onboard the ship (`https://www.mosaic-panorama.org/`) reveal a lead opening close to the ship on that day. Thus, the related decrease of SIC in the high-resolution ASI product on April 17 is possibly real. During the second warm air intrusion, PD for 89 GHz initially decreases again coinciding with rising TWP and LWP values. Only after the event the rise in PD can be observed at all frequencies but strongest at the higher frequencies. Figure 4 (d) illustrates that both the gradient ratio as well as the polarization ratio show higher values after the intrusions (after April 20). The gradient ratio shows even higher values during the intrusions. While the polarization ratio can be considered independent of physical temperature, this is not necessarily the case for the gradient ratio due to different penetration depths (and temperature-dependent permittivities) at 18.7 GHz and 36.5 GHz. Comiso et al. (1997) argue that the effect should be small unless the snow cover emits a sizable fraction of the measured TB. Assuming this is the case for 36.5 GHz we attribute the strong response to rising and decreasing physical temperatures to the strong change in temperature gradients in the snow cover as also depicted later in Figure 5. For sea ice concentration estimates based on polarization differences/gradient ratios, these changes result in (too) low retrieved SIC values as shown in Figure 2 and Figure 3. It is not as straightforward to directly relate the effect of these changes on SIC from OSI-SAF iCDR due to the complex retrieval method. We note however that this algorithm is based on the three-dimensional diagram in TB space of 19V, 37V and 37H, so strong changes in these frequencies relative to each other will affect the retrieval. The OSI-SAF iCDR product provides two uncertainty estimates (algorithm uncertainty and "representativeness" uncertainty, i. e. uncertainty due to resampling and mismatch of footprints at different channels (Lavergne et al., 2019)). Here, the sum of these two uncertainties (gives as one standard deviation) increases from below 2 % before the events to up to 5.6 % on April 21 (not shown) for the collocated data shown in Figure 3, i. e., the uncertainty estimates correctly identify a potential problem in the retrieved SIC.

3.1.1. Atmospheric influence

In the few days after the intrusions, the temperature and TWV were on average higher than before, while LWP is as low as during the first two weeks of April, see Figure 3. Previous studies (Andersen et al., 2007; Oelke, 1997) demonstrated that atmospheric events also can increase retrieved SIC and not only decrease like in our case. Emissions from water vapor or liquid water path contributing to the satellite signal are in general not polarized (Ulaby et al., 2013). This decreases PD, which causes an increase in retrieved SIC for algorithms relying on PD (like ASI). This is not observed here: we see an increase in PD after the warm air intrusion events.

Scattered radiation, e. g., by ice particles in clouds, may have a polarized component. However, observations by Troitsky et al. (2003) report values of PD and duration of periods with polarization differences that are too small to explain the development of PD we observe here. Also, compared to the surface emissions, the contribution of the atmosphere is small at the low frequencies 6.9 and 19 GHz and is thus in any case not the most likely candidate for the PD increase. Other factors have to explain the increase in PD. We thus concentrate on explanations related to changed surface emission.

3.2. Snow accumulation and metamorphism

Wagner et al. (2022) describe a significant snowfall event from April 16 – April 21 accompanying the warm air intrusions. Snowfall events could have had an increasing effect on PD due to atmospheric scattering, but we observe the increase *after* the snowfall. A detailed analysis suggests that much of the fresh snowfall during this event may have been lost into leads (Clemens-Sewall et al., 2022b). Even if there was snow accumulation on level ice, we would expect the fresher snow (less dense, refractive index more similar to air) to decrease the PD. For the large-scale area, this snowfall cannot explain the microwave signal. It is important to keep in mind that the surface conditions at the Remote Sensing Site on the MOSAiC floe were not representative for the larger area. Mainly because the instruments themselves posed obstacles and caused artificial snow accumulation. Thus, for the ground-based radiometers the snowfall is relevant in the interpretation (see Section 3.4).

For understanding and modeling the observed microwave emission, temperature profiles of the snow are important. Here we use temperature profiles from simulations with the SNOWPACK model. (Lehning et al., 2002a; Bartelt and Lehning, 2002; Lehning et al., 2002b; Wever et al., 2019) The model was initialized with a snow pit from April 08 and driven with MET tower 2 m air temperature and ERA-5 reanalysis data (Hersbach et al., 2020). For simulating the brightness temperature of the snow/ice system of the MOSAiC floe, density and correlation length from the SMP profiles are used (see section 6.1) together with the temperature profiles from the SNOWPACK simulations. To match the varying snow height of the SMP profiles, simulations with a snowpack of 10 to 30 cm in 5 cm steps were performed. In these simulations, snowfall was omitted. We compared the simulated temperature profiles with snow pit measurements (not shown). The shape of the temperature profiles was well predicted from the SNOWPACK simulations, although we note a slight negative bias ($< -2°$C). Figure 5 shows the simulated snow temperature for a 20 cm deep snowpack. Overall, the snow temperature increased by more than 10°C. After the events, the snow temperature remains higher at the lower part of the snowpack for several days. These data serves as input for the microwave emission modeling presented in Section 3.3.

The changes of the snow microstructure caused by the warm air intrusions are evident when one looks at the SMP profiles shown in Figure 6. It shows the distribution of the SMP profile averages for density (left), SSA (middle) and exponential correlation length (right). The data is split into before (April 08 - April 15) and after (April 20 - April 27) the warming events. A shift towards lower density and SSA and higher correlation length is visible in the data suggesting that the warm air intrusions led to snow metamorphism. The strong and even inverted temperature gradient effects the migration of water vapor (deposition and sublimation) in the snow and we would expect larger snow structures resulting in lower SSA, which is indeed visible in the data. The changes in density are mainly in the upper layers of the snow, possibly related to fresh snow.

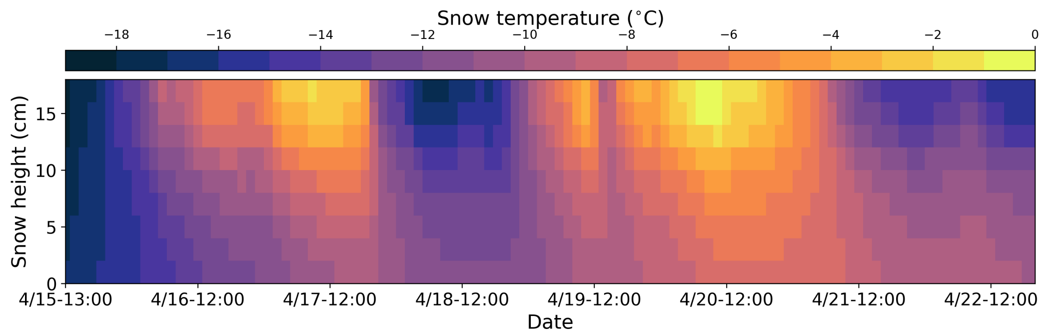

Figure 5: Snow temperature profile from a SNOWPACK simulation initialized with 20 cm of snow.

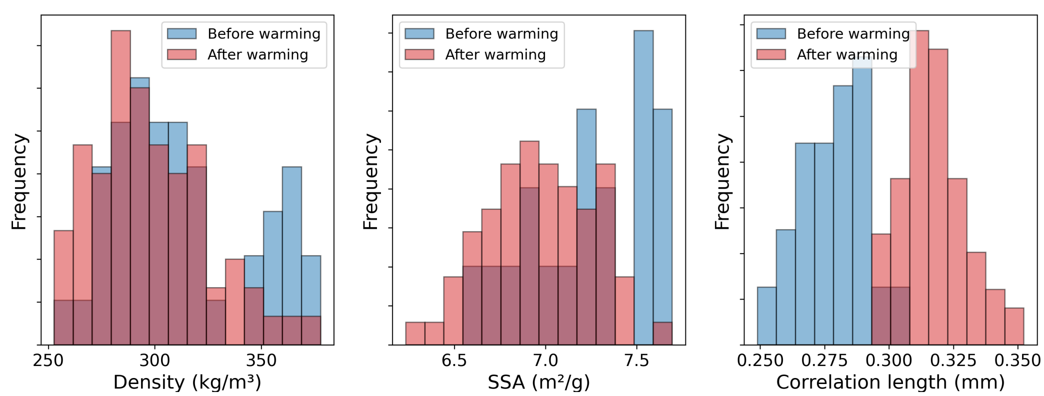

Figure 6: Histogram of the density, SSA and exponential correlation length of the 132 SMP profiles.

The change in increased correlation length affects the scattering strength of the snow: in general higher correlation lengths lead to stronger scattering. On the other hand, higher snow temperatures (Figure 5) increase emissions. To understand how these surface changes affect brightness temperatures in more detail we therefore model the microwave emissions in the following.

3.3. Floe perspective: microwave emission modeling

We further adopt the local perspective by using a statistical approach in modelling the brightness temperatures. If we assume that the SMP measurements are representative of the Central Observatory (of the order of ≈2 km) in terms of statistical distributions of the measured quantities, we should be able to simulate the effect of the warm air intrusions on the microwave signature. A comparison to satellite data is only meaningful on a qualitative level due to the different scales and atmospheric effects.

3.3.1. Brightness temperatures from modelling

We show the modelled polarization ratio of 18.7 GHz (PR(19)), the gradient ratio of 36.5 GHz and 18.7 GHz at vertical polarization (GR(37/19)) and the polarization difference at 89 GHz (PD89) in Figure 7. The model output for the individual frequencies is shown in the supplement (Figure S2). The blue histograms correspond to input profiles from before (April 08 - April 15), while the red histograms show modelled brightness temperatures using profiles from after the warming events (April 21 - April 27). In general, the model output shows a clear increase of brightness temperatures for all frequencies (at both polarizations) except for 36.5 GHz, where the situation is reversed (see Section 6.2). Qualitatively, an increase is also seen in the satellite data, but not for the horizontally-polarized TB at 18.7 GHZ and 36.5 GHz.

When looking at the ratios that are used in many sea ice concentration algorithms, the polarization ratio at 18.7 GHz remains mostly unchanged if no surface glazing is modeled (Figure 7, upper row). GR(37/19) increases noticeable compared to the values prior to the warming events and PD at 89 GHz shows only a slight increase. From a satellite perspective we observe an increase in all three quantities, see Figure 8, which is different from what we observe in the model without glaze ice layer. Understanding the pronounced rise in satellite-measured PD, which causes the strong drop in sea ice concentration from the ASI algorithm, is key for potentially improving such PD based SIC algorithms. As discussed earlier, the change in PD89 cannot be explained by variability in downwelling radiation due to cloud cover and thus must be due to changes of the snow surface which is however not captured by the quantities derived from SMP profiles (density, SSA and correlation length).

3.3.2. Model experiment floe: simulation of a glaze ice layer

Visual observations during the expedition and also the TLS reflectance data (see supplemental material, Figure S3 and Figure S4) suggest the development of a glaze ice layer, which formed in some spots of the ice floe during the first, and almost everywhere during the second warming event. Glaze ice layers at the top of the snowpack can have a strong impact on the microwave emission of the snow (Grenfell and Putkonen, 2008; Mätzler et al., 1984; Rees et al., 2010; Smith, 1996, e.g.). Studies on the effect of such ice layers at the surface of the snowpack have shown that, close to the Brewster angle, they usually have a minor impact on vertically-polarized TB, but strongly influence horizontally-polarized TB (Rees et al., 2010, e.g.,) due to the high dielectric contrast between the snow and the ice layer. Thus, algorithms utilizing polarization differences or ratios (e. g., ASI and NASA-Team) will be influenced by the presence of such layers. How strong a certain frequency is impacted depends generally on the thickness of the ice layer (Montpetit et al., 2013, e.g.,). When we include such an ice layer in the SMP-based modelling, the modelled data (Figure 7 bottom row) shows relative changes (increase in PR(19) and PD89) that are comparable to the ones observed from satellite, see Figure 8. GR(37/19) is hardly effected since it is based on vertically-polarized brightness temperatures.

3.4. Site perspective: ground-based radiometers

We now adopt the site perspective and investigate the ground-based radiometer measurements.

3.4.1. Brightness temperatures from ground-based radiometers

The brightness temperatures of the ground-based radiometers between 15 and 20 April 2020 are summarized in Figure 9. The data is smoothed applying an one hour running mean. The analyzed period can be divided into four phases. The first phase is the period from April 15 to April 17. In this period the first warm air intrusion hit the MOSAiC site. Temperatures are rising from $-12°$C to $-2°$C at 2 m height. Increased wind speed and (wet) snowfall led to changes of the snow cover. This is evident at, e. g., 6.9 GHz horizontal polarization, fluctuations indicate here that surface properties in the FoV of the radiometer changed and that there might

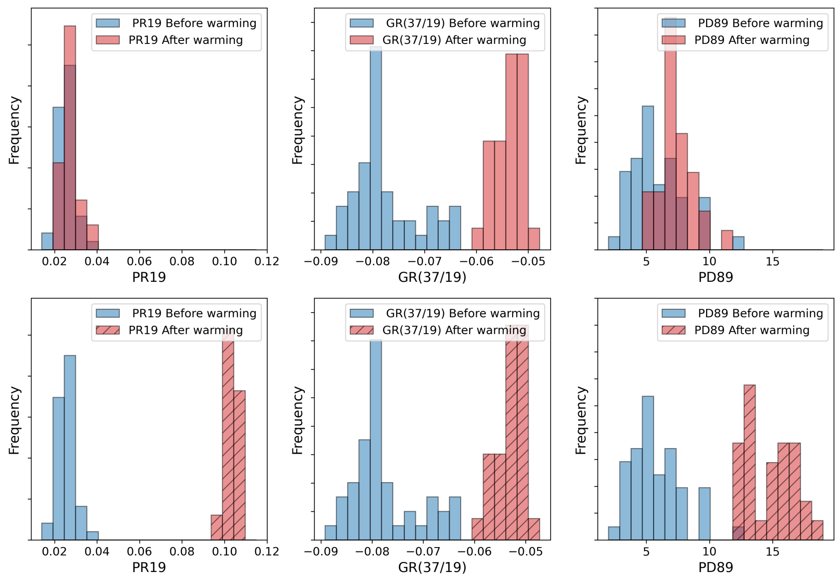

Figure 7: Histogram of simulated PR(19), GR(37/19) and PD89 based on 84 the SMP profiles. The data is split into the periods from April 08 - April 15 (blue) and April 21 - April 27 (red). In the bottom panel, a thin ice layer (2 mm) was added on top of the snow (red, hatched) to simulate the effect of surface glazing after the second warming wave.

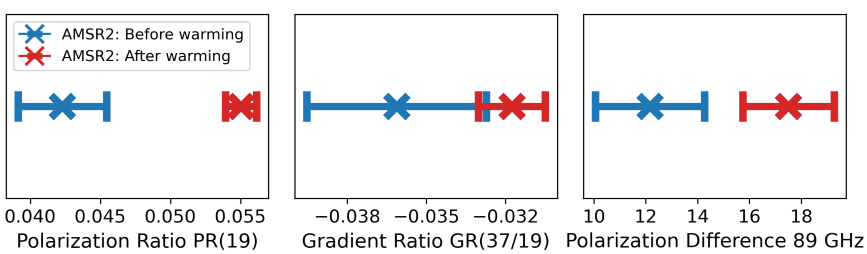

Figure 8: Mean and standard deviation of PR(19), GR(37/19) and PD89 derived from AMSR2 brightness temperatures collocated to *Polarstern* from Figure 4. The data is split into the periods from April 08 - April 15 (blue) and April 21 - April 27 (red) matching the modeled periods shown in Figure 7.

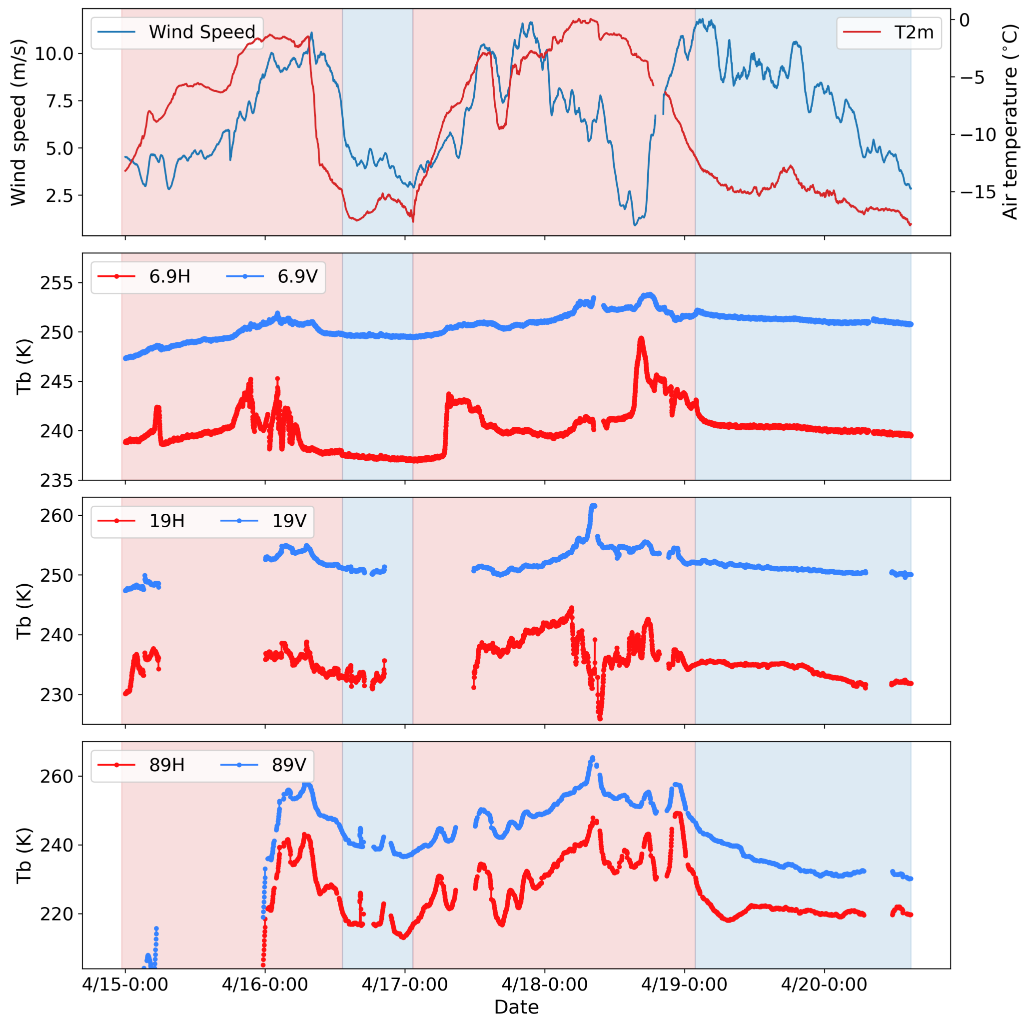

Figure 9: Top: 2 m air temperature and 10 m wind speed during the warm air intrusions. Rows 2 – 4: Observed brightness temperatures for vertical (V) and horizontal (H) polarizations for 6.9 GHz, 19 GHz, and 89 GHz, respectively. Background shading indicate the four different phases for cloudy (red) and clear sky (blue) conditions.

be already some low amount of liquid water building in the uppermost layer of the snowpack. While the average brightness temperature at lower frequencies (6.9 to 19 GHz) is only slightly increasing, a strong increase can be found at 89 GHz, indicating that mainly the temperature of the upper snow layer changed (89 GHz has the lowest penetration depth), which is consistent with Figure 5. Strong short-term fluctuations at 89 GHz are captured well in the simulations and are likely due to fluctuations of reflected downwelling radiation caused by increased cloud cover and higher LWP.

The second phase, between April 17 and April 18 (first blue shading in Figure 9) is marked by a rapid cooling below $-15°$C, clear sky and calm conditions. Brightness temperatures at all frequencies are stable during this phase with a slight cooling at 19 GHz and a strong drop in brightness temperature at 89 GHz.

The third phase marks the second, stronger warm air intrusion where the 2 m air temperature reached $0°$C. Strong changes for horizontally-polarized TB at all frequencies indicate changes in the snow surface due to snow fall and drift as well as accumulation and possible formation of liquid water. However, during this period, increased snow accumulation around the instruments complicate the interpretation of the data at the remote sensing site as the exact timings of snow dune formation are unknown.

Of special interest is the fourth phase, the period right after the second warming event, where a strong decline in brightness temperatures is observed at higher frequencies. At 89 GHz, TB H drops by around $30°$C within 6.5 hours. For vertical polarization, this decrease is less pronounced.

Consequently, PD at 89 GHz shows a strong increase during this period, which is consistent with the increase observed by the satellites (Figure 4). At the lower frequencies, this drop in TB H is less pronounced. In contrast to the satellite observations, the PD 89 of the ground-based observations recovers after less than one day and thus much faster than the satellite measurements. A likely explanation is the accumulation of snow in front of the ground-based radiometers, which does not occur on the satellite scale. This already highlights the need of auxiliary data when using ground-based measurements to interpret satellite data due to the local snow conditions. Unlike the snow drifts that accumulated in front of the instruments, most of the level ice on the floe-scale did not experience accumulation during this event.

3.4.2. Model experiment on-ice site: simulation of a glaze ice layer

Similar to the simulations of the SMP profiles (Section 3.3.2), we perform an experiment with simulating the effect of a glaze ice layer. In the model, the glaze ice layer is approximated by a thin, radiometrically flat ice layer (≤ 1.6 mm) at top of the snowpack. The setup is chosen such that the model can reproduce the observed PD changes from the ground-based radiometer at 6.9 GHz and 89 GHz during phase 4, i. e., the clear sky phase after the second warm air intrusion (right blue shading in Figure 9). As discussed earlier, during this phase, the drop in PD at 89 GHz cannot be explained by cloud forcing and is most likely due to the formation of a glaze ice layer in the FoV of the radiometer.

For the experiment we simulate an ice layer that starts developing at April 20 at around 13:00 and grows up to 1.6 mm until 17:00. After that we allow a layer of new snow to accumulate on top of this ice layer. We know of the increased snow accumulation in front of the instruments due to snow drift formation as wind speed was high during this period (Figure 9), however the exact timing of new snow accumulations remains a reasonable assumption. The reflectance data from the TLS scan on April 22 shows that a glaze ice layer is not visible anymore in the FoV of the radiometers by this date. Figure 10 shows the observed and simulated brightness temperatures between April 20 10:00 and April 21 10:00.

With this set-up it is possible to reproduce the observed increase of polarization difference at 89 GHz indicating that indeed the formation of a glaze ice layer most likely led to the strong increase in observed PD 89.

In summary, the temporal development of microwave brightness temperatures measured by the on-ice radiometers and especially their polarization difference can be explained if a thin glaze ice layer is added in the microwave emission model. Such a glaze layer actually was observed in the field. The effect of the glaze ice layer is larger at higher frequencies and mainly affect the polarization difference.

4. Discussion

The effects of the warm air intrusions on sea ice concentration retrievals are manifold, but we believe we have identified dominant mechanisms for the case study presented here. First, the changed temperature gradients in the snow and snow metamorphism (increase in correlation length). This influences SIC estimates that rely on the gradient ratio GR(37/19). The increase in GR(37/19) is due to the changed snow temperature (gradient) and is not fully compensated for by snow metamorphism (which decreases GR(37/19)). Second, we attribute the strong increase of satellite-measured PD after the warm air events to an ice glazing of the snow surface that was present on a large scale. Such glazing was observed in the field and model results suggest that it can explain the observed satellite microwave

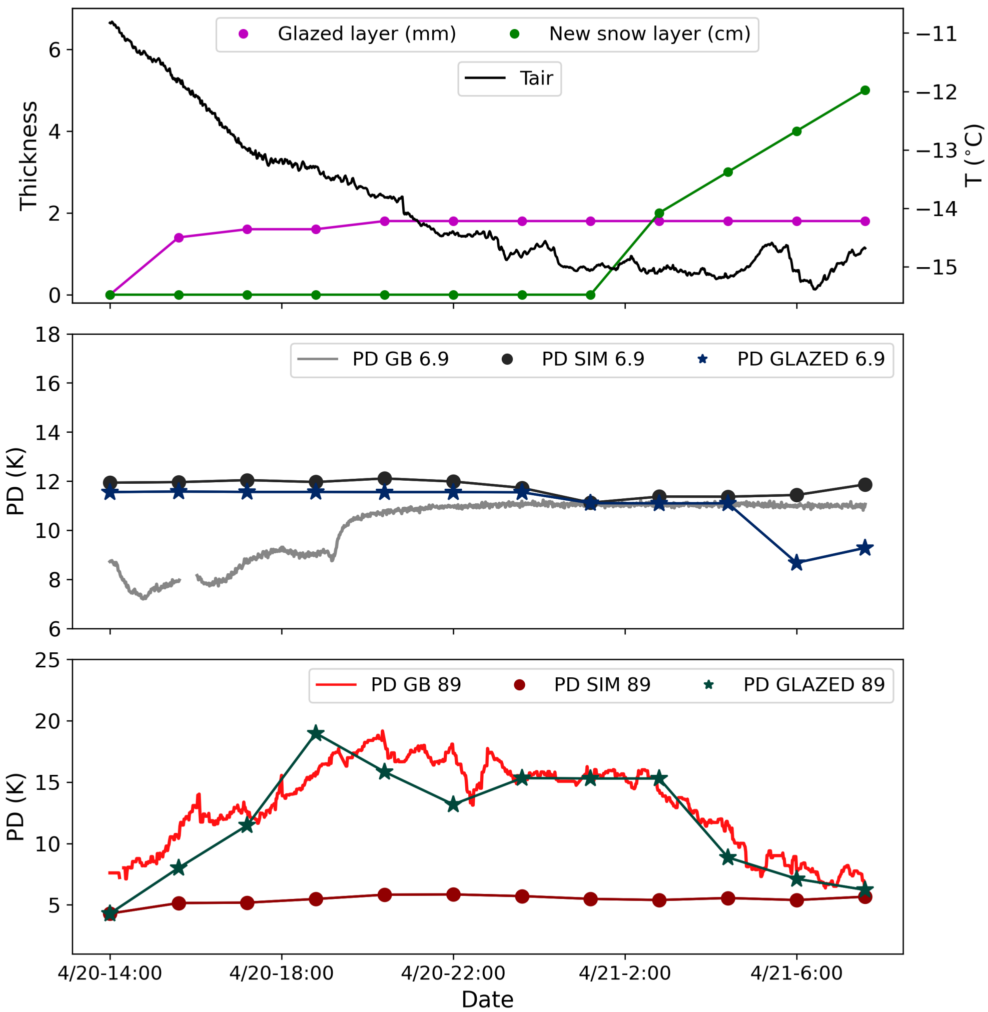

Figure 10: Model experiment adding a glaze ice layer on top of the snowpack covering parts of phase 4 after the second warm air intrusion (2nd blue shading in Figure 9). The top panel shows 2 m air temperature and the glazed and snow layer setup of the experiment. Panel two and three show the observed (solid) and simulated brightness temperatures without (dotted) and with (stars) the glazed layer for PD6.9 (middle) and PD89 (bottom).

brightness temperatures. The higher PD causes a decrease in SIC in some sea ice concentration products that we investigate in this study (significantly for the algorithm that mainly rely on PD89, as ASI does, or PR(19) as NASA TEAM, but also visible for algorithms like OSI-SAF that use the TB space spanned by both polarizations at 36.5 GHz as part of their retrieval; see Section 2.1).

We note a stronger response of the microwave emissions to the warming events at higher frequencies that have smaller penetration depths into the snow. A thin ice crust also effects these frequencies more while the wavelengths of the lower frequencies are large compared to the thickness of the crust. SIC retrievals using vertical polarization or ones that are based on lower frequencies like 6.9 GHz are less affected. For example, the dual algorithm approach of the NSIDC-CDR largely mitigates the glazing impact in this case, as the Bootstrap algorithm gives a high value for SIC. While this is an advantage for the case presented here, this approach might also overestimate sea ice concentration in other situations. For example, the North East Water polynya at the Greenland coast that opened after the events (Figure 2, middle column, first three rows), is hardly visible in the NSIDC-CDR product.

Hypothesizing that such glazing events should increase in a warming Arctic, as not only warm air intrusions but also rain on snow events can cause them, the choice of low frequency / vertical polarization algorithms could be a more robust choice for the future. In the study by Rees et al. (2010) about an ice crust on snow on land 6.9 GHz showed the least response to the ice crust as well. We note that, different to our case, PD at 19 GHz was affected most in their study, which is likely due to a different thickness of the ice crust and different snow conditions.

Modeling snow and ice microwave emission remains a challenge especially at satellite-footprint scale, even if a large amount of observational data is available. Partly this is due to the local heterogeneity making it difficult, e. g., to match radiometer observations and ground-based observations. For example, we did not only observe differences in the snow cover between the ground-based radiometer footprints at the same site but also within one footprint (see supplemental Figure S1). We overcome this problem by using the vast amount of snow profiles, thanks to the SMP measurements, in combination with modelling, providing a statistical description of expected surface brightness temperatures (Figure 7). Still, if the radiometers measure snow conditions that are not representative of the surroundings (due to snow accumulation), comparisons to these TB measurements are impeded. The statistical description might be more comparable to a satellite observation in case of negligible atmospheric effects. However we cannot be certain that the SMP data are representative of a satellite footprint of the order of tens of kilometres. Also, certain parameters, such as surface roughness that are important for emission modeling of satellite observations, are not directly available. Coherence effects, that depend on frequency and layer thickness, are another source of uncertainty. Nevertheless, the temporal evolution of the ground-based radiometer measurements can be reproduced by a microwave emission model if the glaze ice layer is included. Similarly, including a glaze layer allows us to qualitatively model relative changes as observed from space using the SMP measurements as input. This is one of the few existing cases where a false change in satellite SIC can be fully explained by the observed surface changes from ground-based measurements (snow and ice physics and radiometers). We are confident that adopting the three perspectives from the different scales (satellite, floe, site) allowed for a plausible interpretation of the observations.

5. Conclusion

Arctic amplification, i. e., the more rapid and stronger increase of temperatures in the Arctic compared to low latitudes (Serreze and Barry, 2011; Screen and Simmonds, 2010; Comiso and Hall, 2014; Wendisch et al., 2017, 2023), can lead to an increased occurrence of warm air intrusions (Graham et al., 2017).

As shown in this study, they can affect brightness temperatures measured by satellite microwave radiometers and cause uncertainties in the derived sea ice concentration products. In our case, the warm air intrusions led to a large-scale spurious strong decrease in SIC and an increase in the deviations between different SIC products. These deviations lasted for several days. Only one climate data record was little affected. It, however, has the tendency to always produce high SIC values, which was the correct solution in this case.

We offer an interpretation of the signals based on observations from the MOSAiC expedition and by microwave emission modeling, taking into account atmospheric effects as well as surface snow metamorphism. As an explanation for the changed microwave emissions during and after the warming events, we propose the formation of a large-scale glaze ice layer, which is persistent even days after the warm air intrusion.

Many recent sea ice concentration studies, (Lu et al., 2022, e. g.,), focus on the influence of the atmosphere on ice concentration. In our case, the surface changes are highly relevant and should be included in future evaluations of sea ice concentration retrieval algorithms. Especially, near 90 GHz algorithms were thought to be less sensitive to these surface effects like ice lenses within the snow because of their small penetration depth compared to the lower frequencies (Ivanova et al., 2015). However, as shown in this study, certain surface effects like glazing can have a strong influence on these algorithms. Identifying similar events, their scale in time and space and their frequency of occurrences can provide additional insights to quantify whether this effect is significant on longer temporal and spatial scales and for climate data records. This is also interesting for past sea ice concentration datasets and inter-comparison studies of sea ice concentration algorithms. In the future, due to a projected increase in such warm air intrusions, the relevance of their effects on sea ice climate records from satellites and the distinction between actual influence of climate warming on sea ice, as described by, e. g., Merkouriadi et al. (2020), and retrieval uncertainties will become more important. Regarding the estimation of product uncertainties this needs consideration as well, possibly by using dynamic uncertainty estimates, i. e., uncertainties that are neither constant nor only dependent on SIC. A good example is the OSI-SAF iCDR product that provides such estimates which show an increased uncertainty after the events.

The detailed MOSAiC measurements allowed for a sophisticated emission model setup to simulate the ground-based radiometer data that enabled us to interpret the observed satellite changes. When considering ice concentration algorithms based on physical forward models, however, it is not yet feasible to fully account for the variability of surface emissions due to the high variability and amount of needed input parameters as well as model physics limitations.

Instead, multi-frequency methods exploiting the synergy of the robustness of 6.9 GHz and the high spatial resolution of 89 GHz are a promising approach for future retrievals. Upcoming satellite missions like the Copernicus Imaging Microwave Radiometer (CIMR) (Donlon, 2020) will provide measurements at 6.9 GHz at a much higher spatial resolution (around 15 km) than current satellite sensors, which makes it well suited for sea ice concentration retrievals at higher spatial resolution (5 km at 37 GHz) and higher accuracy (using 6.9 GHz) than what is available today.

References

Alfred-Wegener-Institut Helmholtz-Zentrum für Polar- und Meeresforschung. 2017. Polar Research and Supply Vessel POLARSTERN Operated by the Alfred-Wegener-Institute. *Journal of large-scale research facilities* **3**(A119). doi:10.17815/jlsrf-3-163. Rainer Knust.

Andersen, S, Tonboe, R, Kaleschke, L, Heygster, G, Pedersen, LT. 2007. Intercomparison of passive microwave sea ice concentration retrievals over the high-concentration Arctic sea ice. *Journal of Geophysical Research: Oceans* **112**(C8). doi:https://doi.org/10.1029/2006JC003543.

Andersen, S, Tonboe, R, Kern, S, Schyberg, H. 2006. Improved retrieval of sea ice total concentration from spaceborne passive microwave observations using numerical weather prediction model fields: An intercomparison of nine algorithms. *Remote Sensing of Environment* **104**(4): 374–392. ISSN 0034-4257. doi:https://doi.org/10.1016/j.rse.2006.05.013.

Aue, L, Vihma, T, Uotila, P, Rinke, A. 2022. New Insights Into Cyclone Impacts on Sea Ice in the Atlantic Sector of the Arctic Ocean in Winter. *Geophysical Research Letters* **49**(22): e2022GL100051. doi:https://doi.org/10.1029/2022GL100051.

Bartelt, P, Lehning, M. 2002. A physical SNOWPACK model for the Swiss avalanche warning Part I: numerical model. *Cold Regions Science and Technology* **35**: 123–145.

Cavalieri, DJ, Gloersen, P, Campbell, WJ. 1984. Determination of sea ice parameters with the NIMBUS 7 SMMR. *Journal of Geophysical Research: Atmospheres* **89**: 5355–5369. ISSN 2156-2202. doi:10.1029/JD089iD04p05355.

Cavalieri, DJ, Parkinson, CL, Gloersen, P, Zwally, HJ. 1997. Arctic and Antarctic Sea Ice Concentrations from Multichannel Passive-Microwave Satellite Data Sets: October 1978-September 1995 User's Guide. NASA Goddard Space Flight Center. `https://ntrs.nasa.gov/citations/19980076134`.

Choudhury, BJ, Schmugge, TJ, Chang, A, Newton, RW. 1979. Effect of surface roughness on the microwave emission from soils. *Journal of Geophysical Research: Oceans* **84**(C9): 5699–5706. doi:https://doi.org/10.1029/JC084iC09p05699.

Clemens-Sewall, D. 2021. Terrestrial Laser Scans of the on-ice Remote Sensing instrument site on the Multidisciplinary Drifting Observatory for the Study of Arctic Climate (MOSAiC) in April 2020 (Leg 3). doi:doi:10.18739/A25717P9Q. Arctic Data Center.

Clemens-Sewall, D, Parno, M, Perovich, D, Polashenski, C, Raphael, IA. 2022a. FlakeOut: A geometric approach to remove wind-blown snow from terrestrial laser scans. *Cold Regions Science and Technology* **201**: 103611. ISSN 0165-232X. doi:10.1016/j.coldregions.2022.103611. `https://www.sciencedirect.com/science/article/pii/S0165232X22001306`.

Clemens-Sewall, D, Polashenski, C, Frey, MM, Cox, CJ, Granskog, MA, Macfarlane, AR, Fons, SW, Schmale, J, Hutchings, JK, von Albedyll, L, Arndt, S, Perovich, D. 2022b. Snow Loss into Leads in Arctic Sea Ice: Minimal in Typical Wintertime Conditions, but High During a Warm and Windy Snowfall Event. Submitted.

Clemens-Sewall, D, Polashenski, C, Raphael, I, Perovich, D, Fons, S, Itkin, P, Jaggi, M, Jutila, A, Macfarlane, A, Matero, I, Oggier, M, Wagner, D, Visser, R, Olufson, T, Radenz, M, Schönning, C, Hansen, J, Votvik, M, Brossier, E, Svavarsdottir, S. 2022c. High-Resolution Repeat Topography of Drifting Ice Floes in the Arctic Ocean from Terrestrial Laser Scanning Collected on the Multidisciplinary drifting Observatory for the Study of Arctic Climate Expedition. NSF Arctic Data Center. doi:10.18739/A26688K9D. Medium: text/xml Type: dataset. `https://arcticdata.io/catalog/view/doi:10.18739/A26688K9D`.

Colliander, A, Lahtinen, J, Tauriainen, S, Pihlflyckt, J, Lemmetyinen, J, Hallikainen, M. 2007. Sensitivity of Airborne 36,5-GHz Polarimetric Radiometer's Wind-Speed Measurement to Incidence Angle. *IEEE Transactions on Geoscience and Remote Sensing* **45**(7): 2122–2129. ISSN 0196-2892.

Comiso, JC. 1986. Characteristics of Arctic winter sea ice from satellite multispectral microwave observations. *Journal of Geophysical Research: Oceans* **91**(C1): 975–994. doi:https://doi.org/10.1029/JC091iC01p00975.

Comiso, JC, Cavalieri, DJ, Parkinson, CL, Gloersen, P. 1997. Passive microwave algorithms for sea ice concentration: A comparison of two techniques. *Remote Sensing of Environment* **60**(3): 357–384. ISSN 0034-4257. doi:10.1016/S0034-4257(96)00220-9.

Comiso, JC, Gersten, RA, Stock, LV, Turner, J, Perez, GJ, Cho, K. 2017. Positive Trend in the Antarctic Sea Ice Cover and Associated Changes in Surface Temperature. *Journal of Climate* **30**(6): 2251 – 2267. doi:10.1175/JCLI-D-16-0408.1.

Comiso, JC, Hall, DK. 2014. Climate trends in the Arctic as observed from space. *WIREs Climate Change* **5**(3): 389–409. ISSN 1757-7799. doi:10.1002/wcc.277.

Cox, C, Gallagher, M, Shupe, M, Persson, O, Solomon, A, Blomquist, B, Brooks, I, Costa, D, Gottas, D, Hutchings, J, Osborn, J, Morris, S, Preusser, A, Uttal, T. 2021. 10-meter (m) meteorological flux tower measurements (Level 1 Raw), Multidisciplinary Drifting Observatory for the Study of Arctic Climate (MOSAiC), central Arctic, October 2019 - September 2020. doi:https://doi.org/10.18739/A2VM42Z5F. Arctic Data Center.

Dada, L, Angot, H, Beck, I, Baccarini, A, Quéléver, LLJ, Boyer, M, Laurila, T, Brasseur, Z, Jozef, G, de Boer, G, Shupe, MD, Henning, S, Bucci, S, Dütsch, M, Stohl, A, Petäjä, T, Daellenbach, KR, Jokinen, T, Schmale, J. 2022. A central arctic extreme aerosol event triggered by a warm air-mass intrusion. *Nature Communications* **13**. ISSN 2041-1723. doi:10.1038/s41467-022-32872-2.

Deems, JS, Painter, TH, Finnegan, DC. 2013. Lidar measurement of snow depth: a review. *Journal of Glaciology* **59**(215): 467–479. ISSN 0022-1430, 1727-5652. doi:10.3189/2013JoG12J154. Publisher: Cambridge University Press.

Derksen, C, Toose, P, Lemmetyinen, J, Pulliainen, J, Langlois, A, Rutter, N, Fuller, M. 2012. Evaluation of passive microwave brightness temperature simulations and snow water equivalent retrievals through a winter season. *Remote Sensing of Environment* **117**: 236–248. ISSN 0034-4257. doi: https://doi.org/10.1016/j.rse.2011.09.021. Remote Sensing of Urban Environments.

Donlon, C. 2020. Copernicus Imaging Microwave Radiometer (CIMR) Mission Requirements Document. Noordwijk, The Netherlands: European Space Agency. Issue Number 4, Version 4.0.

EUMETSAT Ocean and Sea Ice Satellite Application Facility. 2017. *Global sea ice concentration interim climate data record 2016-onwards (v2.0, 2017), OSI-430-b*. EUMETSAT Ocean and Sea Ice Satellite Application Facility. (Data extracted from OSI SAF FTP server/EUMETSAT Data Center: April 2020, Northern Hemisphere). Accessed September 7th, 2021.

Fox-Kemper, B, Hewitt, H, Xiao, C, Aðalgeirsdóttir, G, Drijfhout, S, Edwards, T, Golledge, N, Hemer, M, Kopp, R, Krinner, G, Mix, A, Notz, D, Nowicki, S, Nurhati, I, Ruiz, L, Sallée, JB, andY Yu, AS. 2021. Ocean, Cryosphere and Sea Level Change., in Masson-Delmotte, V, Zhai, P, Pirani, A, Connors, S, Péan, C, Berger, S, Caud, N, Chen, Y, Goldfarb, L, Gomis, M, Huang, M, Leitzell, K, Lonnoy, E, Matthews, J, Maycock, T, Waterfield, T, Yelekçi, O, Yu, R, , Zhoue, B, eds., *In Climate Change 2021: The Physical Science Basis. Contribution of Working Group I to the Sixth Assessment Report of the Intergovernmental Panel on Climate Change*. Cambridge University Press. In Press.

Graham, RM, Cohen, L, Petty, AA, Boisvert, LN, Rinke, A, Hudson, SR, Nicolaus, M, Granskog, MA. 2017. Increasing frequency and duration of Arctic winter warming events. *Geophysical Research Letters* **44**(13): 6974–6983. ISSN 1944-8007. doi:10.1002/2017GL073395.

Grenfell, TC, Putkonen, J. 2008. A method for the detection of the severe rain-on-snow event on Banks Island, October 2003, using passive microwave remote sensing. *Water Resources Research* **44**(3).

Hallikainen, M, Kemppinen, M, Rautiainen, K, Pihlflyckt, J, Lahtinen, J, Tirri, T, Mononen, I, Auer, T. 1996. Airborne 14-channel microwave radiometer HUTRAD. pp. 2285 – 2287 vol.4. doi:10.1109/IGARSS.1996.516963.

Hao, M, Luo, Y, Lin, Y, Zhao, Z, Wang, L, Huang, J. 2019. Contribution of atmospheric moisture transport to winter Arctic warming. *International Journal of Climatology* **39**(5): 2697–2710. doi:https://doi.org/10.1002/joc.5982.

Henderson, GR, Barrett, BS, Wachowicz, LJ, Mattingly, KS, Preece, JR, Mote, TL. 2021. Local and Remote Atmospheric Circulation Drivers of Arctic Change: A Review. *Frontiers in Earth Science* **9**: 549. doi:10.3389/feart.2021.709896.

Hersbach, H, Bell, B, Berrisford, P, Hirahara, S, Horányi, A, Muñoz-Sabater, J, Nicolas, J, Peubey, C, Radu, R, Schepers, D, Simmons, A, Soci, C, Abdalla, S, Abellan, X, Balsamo, G, Bechtold, P, Biavati, G, Bidlot, J, Bonavita, M, Chiara, GD, Dahlgren, P, Dee, D, Diamantakis, M, Dragani, R, Flemming, J, Forbes, R, Fuentes, M, Geer, A, Haimberger, L, Healy, S, Hogan, RJ, Hólm, E, Janisková, M, Keeley, S, Laloyaux, P, Lopez, P, Lupu, C, Radnoti, G, Rosnay, Pd, Rozum, I, Vamborg, F, Villaume, S, Thépaut, JN. 2020. The ERA5 global reanalysis. *Quarterly Journal of the Royal Meteorological Society* **146**(730): 1999–2049. ISSN 1477-870X. doi:10.1002/qj.3803.

Hyland, RW, Wexler, A. 1983. FORMULATIONS FOR THE THERMODYNAMIC PROPERTIES OF THE SATURATED PHASES OF H2O FROM 173.15 TO 473.15 K. *Ashrae Transactions* **89**: 500–520.

Ivanova, N, Pedersen, LT, Tonboe, RT, Kern, S, Heygster, G, Lavergne, T, Sørensen, A, Saldo, R, Dybkjær, G, Brucker, L, Shokr, M. 2015. Intercomparison and evaluation of sea ice algorithms: towards further identification of challenges and optimal approach using passive microwave observations. *The Cryosphere* **9**(5): 1797–1817. ISSN 1994-0416. doi:10.5194/tc-9-1797-2015.

Kaleschke, L, Lüpkes, C, Vihma, T, Haarpaintner, J, Bochert, A, Hartmann, J, Heygster, G. 2001. SSM/I Sea Ice Remote Sensing for Mesoscale Ocean-Atmosphere Interaction Analysis. *Canadian Journal of Remote Sensing* **27**(5): 526–537. ISSN 0703-8992. doi:10.1080/07038992.2001.10854892.

Kaltenborn, J, Macfarlane, AR, Clay, V, Schneebeli, M. 2022. Automatic classification and segmentation of Snow Micro Penetrometer profiles with machine learning algorithms. *EGUsphere* **2022**: 1–30. doi:10.5194/egusphere-2022-938.

King, J, Howell, S, Brady, M, Toose, P, Derksen, C, Haas, C, Beckers, J. 2020. Local-scale variability of snow density on Arctic sea ice. *The*

Cryosphere **14**(12): 4323–4339. doi:10.5194/tc-14-4323-2020. https://tc.copernicus.org/articles/14/4323/2020/.

Lavergne, T, Sørensen, AM, Kern, S, Tonboe, R, Notz, D, Aaboe, S, Bell, L, Dybkjær, G, Eastwood, S, Gabarro, C, Heygster, G, Killie, MA, Brandt Kreiner, M, Lavelle, J, Saldo, R, Sandven, S, Pedersen, LT. 2019. Version 2 of the EUMETSAT OSI SAF and ESA CCI sea-ice concentration climate data records. *The Cryosphere* **13**(1): 49–78. doi:10.5194/tc-13-49-2019.

Lavergne, T, Tonboe, R, Lavelle, J, Eastwood, S. 2016. *Algorithm Theoretical Basis Document for the OSI SAF Global Sea Ice Concentration Climate Data Record*. EUMETSAT Ocean and Sea Ice Satellite Application Facility. Version 1.1.

Lehning, M, Bartelt, P, Brown, B, Fierz, C. 2002a. A physical SNOWPACK model for the Swiss avalanche warning Part III: meteorological forcing, thin layer formation and evaluation. *Cold Regions Science and Technology* **35**: 169–184.

Lehning, M, Bartelt, P, Brown, B, Fierz, C, Satyawali, P. 2002b. A physical SNOWPACK model for the Swiss avalanche warning Part II: Snow microstructure. *Cold Regions Science and Technology* **35**: 147–167.

Lemmetyinen, J, Derksen, C, Pulliainen, J, Strapp, W, Toose, P, Walker, A, Tauriainen, S, Pihlflyckt, J, Karna, JP, Hallikainen, MT. 2009. A Comparison of Airborne Microwave Brightness Temperatures and Snowpack Properties Across the Boreal Forests of Finland and Western Canada. *IEEE Transactions on Geoscience and Remote Sensing* **47**(3): 965–978. doi:10.1109/TGRS.2008.2006358.

Liu, G, Curry, JA. 2003. Observation and interpretation of microwave cloud signatures over the Arctic ocean during winter. *J Appl Meteorol* **42**: 51–64. doi:10.1175/1520-0450(2003)042<0051:OAIOMC>2.0.CO;2.

Lu, J, Scarlat, R, Heygster, G, Spreen, G. 2022. Reducing Weather Influences on an 89 GHz Sea Ice Concentration Algorithm in the Arctic Using Retrievals From an Optimal Estimation Method. *Journal of Geophysical Research: Oceans* **127**(9): e2019JC015912. doi:https://doi.org/10.1029/2019JC015912. E2019JC015912 2019JC015912. https://agupubs.onlinelibrary.wiley.com/doi/abs/10.1029/2019JC015912.

Macfarlane, AR, Schneebeli, M, Dadic, R, Wagner, DN, Arndt, S, Clemens-Sewall, D, Hämmerle, S, Hannula, HR, Jaggi, M, Kolabutin, N, Krampe, D, Lehning, M, Matero, I, Nicolaus, M, Oggier, M, Pirazzini, R, Polashenski, C, Raphael, I, Regnery, J, Shimanchuck, E, Smith, MM, Tavri, A. 2021.

Snowpit SnowMicroPen (SMP) force profiles collected during the MOSAiC expedition. PANGAEA. doi:10.1594/PANGAEA.935554. `https://doi.org/10.1594/PANGAEA.935554`.

Maeda, T, Taniguchi, Y, Imaoka, K. 2016. GCOM-W1 AMSR2 Level 1R Product: Dataset of Brightness Temperature Modified Using the Antenna Pattern Matching Technique. *IEEE Transactions on Geoscience and Remote Sensing* **54**(2): 770–782. doi:10.1109/TGRS.2015.2465170.

Maturilli, M, Holdridge, DJ, Dahlke, S, Graeser, J, Sommerfeld, A, Jaiser, R, Deckelmann, H, Schulz, A. 2021. Initial radiosonde data from 2019-10 to 2020-09 during project MOSAiC. *Alfred Wegener Institute, Helmholtz Centre for Polar and Marine Research, Bremerhaven* doi:10.1594/PANGAEA.928656. Publisher: PANGAEA Type: dataset, Accessed: 03-30-2021.

Mech, M, Maahn, M, Kneifel, S, Ori, D, Orlandi, E, Kollias, P, Schemann, V, Crewell, S. 2020. PAMTRA 1.0: the Passive and Active Microwave radiative TRAnsfer tool for simulating radiometer and radar measurements of the cloudy atmosphere. *Geoscientific Model Development* **13**(9): 4229–4251. doi:10.5194/gmd-13-4229-2020.

Meier, WN, Fetterer, F, Windnagel, AK, Stewart, S. 2021. NOAA/NSIDC Climate Data Record of Passive Microwave Sea Ice Concentration, Version 4. *Boulder, Colorado, USA* doi:oi.org/10.7265/efmz-2t65. Publisher: NSIDC: National Snow and Ice Data Center Type: dataset, Accessed: 2022-09-18.

Meier, WN, Stroeve, JC. 2022. An Updated Assessment of the Changing Arctic Sea Ice Cover. *Oceanography* **35**(3-4): 10 – 19. doi:https://doi.org/10.5670/oceanog.2022.114.

Melsheimer, C. 2019. *ASI Version 5 Sea Ice Concentration User Guide*. Institute of Environmental Physics, University of Bremen. Version 0.9.2.

Meredith, M, Sommerkorn, M, Cassotta, S, Derksen, C, Ekaykin, A, Hollowed, A, Kofinas, G, Mackintosh, A, Melbourne-Thomas, J, Muelbert, M, Ottersen, G, Pritchard, H, Schuur, E. 2019. 2019: Polar Regions., in Pörtner, HO, Roberts, D, Masson-Delmotte, V, Zhai, P, Tignor, M, Poloczanska, E, Mintenbeck, K, Alegría, A, Nicolai, M, Okem, A, Petzold, J, Rama, B, Weye, N, eds., *IPCC Special Report on the Ocean and Cryosphere in a Changing Climate*.

Merkouriadi, I, Cheng, B, Hudson, S, Granskog, M. 2020. Effect of frequent winter warming events (storms) and snow on sea-ice growth – a case from the Atlantic sector of the Arctic Ocean during the N-ICE2015 campaign. *Annals of Glaciology* **61**: 1–7. doi:10.1017/aog.2020.25.

Montpetit, B, Royer, A, Roy, A, Langlois, A, Derksen, C. 2013. Snow Microwave Emission Modeling of Ice Lenses Within a Snowpack Using the Microwave

Emission Model for Layered Snowpacks. *IEEE Transactions on Geoscience and Remote Sensing* **51**(9): 4705–4717. doi:10.1109/TGRS.2013.2250509.

Mätzler, C, Ramseier, R, Svendsen, E. 1984. Polarization effects in seaice signatures. *IEEE Journal of Oceanic Engineering* **9**(5): 333–338. doi:10.1109/JOE.1984.1145646.

Nicolaus, M, Perovich, DK, Spreen, G, Granskog, MA, von Albedyll, L, Angelopoulos, M, Anhaus, P, Arndt, S, Belter, HJ, Bessonov, V, Birnbaum, G, Brauchle, J, Calmer, R, Cardellach, E, Cheng, B, Clemens-Sewall, D, Dadic, R, Damm, E, de Boer, G, Demir, O, Dethloff, K, Divine, DV, Fong, AA, Fons, S, Frey, MM, Fuchs, N, Gabarró, C, Gerland, S, Goessling, HF, Gradinger, R, Haapala, J, Haas, C, Hamilton, J, Hannula, HR, Hendricks, S, Herber, A, Heuzé, C, Hoppmann, M, Høyland, KV, Huntemann, M, Hutchings, JK, Hwang, B, Itkin, P, Jacobi, HW, Jaggi, M, Jutila, A, Kaleschke, L, Katlein, C, Kolabutin, N, Krampe, D, Kristensen, SS, Krumpen, T, Kurtz, N, Lampert, A, Lange, BA, Lei, R, Light, B, Linhardt, F, Liston, GE, Loose, B, Macfarlane, AR, Mahmud, M, Matero, IO, Maus, S, Morgenstern, A, Naderpour, R, Nandan, V, Niubom, A, Oggier, M, Oppelt, N, Pätzold, F, Perron, C, Petrovsky, T, Pirazzini, R, Polashenski, C, Rabe, B, Raphael, IA, Regnery, J, Rex, M, Ricker, R, Riemann-Campe, K, Rinke, A, Rohde, J, Salganik, E, Scharien, RK, Schiller, M, Schneebeli, M, Semmling, M, Shimanchuk, E, Shupe, MD, Smith, MM, Smolyanitsky, V, Sokolov, V, Stanton, T, Stroeve, J, Thielke, L, Timofeeva, A, Tonboe, RT, Tavri, A, Tsamados, M, Wagner, DN, Watkins, D, Webster, M, Wendisch, M. 2022. Overview of the MOSAiC expedition: Snow and sea ice. *Elementa: Science of the Anthropocene* **10**(1). ISSN 2325-1026. doi:10.1525/elementa.2021.000046.

Nixdorf, U, Dethloff, K, Rex, M, Shupe, M, Sommerfeld, A, Perovich, DK, Nicolaus, M, Heuzé, C, Rabe, B, Loose, B, et al. 2021. MOSAiC Extended Acknowledgement. Zenodo. doi:10.5281/zenodo.5179739.

Nomokonova, T, Ebell, K, Löhnert, U, Maturilli, M, Ritter, C, O'Connor, E. 2019. Statistics on clouds and their relation to thermodynamic conditions at Ny-Ålesund using ground-based sensor synergy. *Atmospheric Chemistry and Physics* **19**(6): 4105–4126. doi:10.5194/acp-19-4105-2019.

Oelke, C. 1997. Atmospheric signatures in sea-ice concentration estimates from passive microwaves: Modelled and observed. *International Journal of Remote Sensing* **18**: 1113–1136.

Onstott, RG, Grenfell, TC, Matzler, C, Luther, CA, Svendsen, EA. 1987. Evolution of microwave sea ice signatures during early summer and midsummer in the marginal ice zone. *Journal of Geophysical Research: Oceans* **92**(C7):

6825–6835. doi:https://doi.org/10.1029/JC092iC07p06825.
Perovich, DK, Meier, T, W, M, SL, Farrell, Hendricks, S, Gerland, S, et al. 2017. Sea ice, Arctic report card 2017.
Proksch, M, Löwe, H, Schneebeli, M. 2015. Density, specific surface area, and correlation length of snow measured by high-resolution penetrometry. *Journal of Geophysical Research: Earth Surface* **120**(2): 346–362. doi:https://doi.org/10.1002/2014JF003266.
Rabe, B, Heuzé, C, Regnery, J, Aksenov, Y, Allerholt, J, Athanase, M, Bai, Y, Basque, C, Bauch, D, Baumann, TM, Chen, D, Cole, ST, Craw, L, Davies, A, Damm, E, Dethloff, K, Divine, DV, Doglioni, F, Ebert, F, Fang, YC, Fer, I, Fong, AA, Gradinger, R, Granskog, MA, Graupner, R, Haas, C, He, H, He, Y, Hoppmann, M, Janout, M, Kadko, D, Kanzow, T, Karam, S, Kawaguchi, Y, Koenig, Z, Kong, B, Krishfield, RA, Krumpen, T, Kuhlmey, D, Kuznetsov, I, Lan, M, Laukert, G, Lei, R, Li, T, Torres-Valdés, S, Lin, L, Lin, L, Liu, H, Liu, N, Loose, B, Ma, X, McKay, R, Mallet, M, Mallett, RDC, Maslowski, W, Mertens, C, Mohrholz, V, Muilwijk, M, Nicolaus, M, O'Brien, JK, Perovich, D, Ren, J, Rex, M, Ribeiro, N, Rinke, A, Schaffer, J, Schuffenhauer, I, Schulz, K, Shupe, MD, Shaw, W, Sokolov, V, Sommerfeld, A, Spreen, G, Stanton, T, Stephens, M, Su, J, Sukhikh, N, Sundfjord, A, Thomisch, K, Tippenhauer, S, Toole, JM, Vredenborg, M, Walter, M, Wang, H, Wang, L, Wang, Y, Wendisch, M, Zhao, J, Zhou, M, Zhu, J. 2022. Overview of the MOSAiC expedition: Physical oceanography. *Elementa: Science of the Anthropocene* **10**(1). ISSN 2325-1026. doi:10.1525/elementa.2021.00062. `https://doi.org/10.1525/elementa.2021.00062`.
Radiometrics. 2004. AC1900 19 GHz, AC3700 37 GHz, and AC8900 89 GHz dual polarization radiometers. *Radiometric Corporation* .
Rees, A, Lemmetyinen, J, Derksen, C, Pulliainen, J, English, M. 2010. Observed and modelled effects of ice lens formation on passive microwave brightness temperatures over snow covered tundra. *Remote Sensing of Environment* **114**(1): 116–126. ISSN 0034-4257. doi:https://doi.org/10.1016/j.rse.2009.08.013.
Rinke, A, Cassano, JJ, Cassano, EN, Jaiser, R, Handorf, D. 2021. Meteorological conditions during the MOSAiC expedition: Normal or anomalous? *Elementa: Science of the Anthropocene* **9**(1). ISSN 2325-1026. doi:10.1525/elementa.2021.00023.
Rinke, A, Maturilli, M, Graham, RM, Matthes, H, Handorf, D, Cohen, L, Hudson, SR, Moore, JC. 2017. Extreme cyclone events in the Arctic: Wintertime variability and trends. *Environmental Research Letters* **12**(9): 094006. ISSN

1748-9326. doi:10.1088/1748-9326/aa7def. Publisher: IOP Publishing.

Scambos, T, Frezzotti, M, Haran, T, Bohlander, J, Lenaerts, J, Van Den Broeke, M, Jezek, K, Long, D, Urbini, S, Farness, K, et al. 2012. Extent of low-accumulation 'wind glaze' areas on the East Antarctic plateau: implications for continental ice mass balance. *Journal of Glaciology* **58**(210): 633–647. doi:10.3189/2012JoG11J232.

Schreiber, EAP, Serreze, MC. 2020. Impacts of synoptic-scale cyclones on Arctic sea-ice concentration: a systematic analysis. *Annals of Glaciology* **61**(82): 139–153. doi:10.1017/aog.2020.23.

Screen, JA, Simmonds, I. 2010. The central role of diminishing sea ice in recent Arctic temperature amplification. *Nature* **464**(7293): 1334–1337. ISSN 1476-4687. doi:10.1038/nature09051.

Semmler, T, McGrath, R, Wang, S. 2012. The impact of Arctic sea ice on the Arctic energy budget and on the climate of the Northern mid-latitudes. *Clim Dyn* **39**: 2675–2694. doi:https://doi.org/10.1007/s00382-012-1353-9.

Serreze, MC, Barry, RG. 2011. Processes and impacts of Arctic amplification: A research synthesis. *Global and Planetary Change* **77**(1): 85–96. ISSN 0921-8181. doi:https://doi.org/10.1016/j.gloplacha.2011.03.004.

Shi, Y. 2019. Atmospheric Radiation Measurement (ARM) user facility. Surface Meteorological Instrumentation (PWD). 2019-10-11 to 2020-10-01, ARM Mobile Facility (MOS) MOSAIC (Drifting Obs - Study of Arctic Climate); AMF2 (M1). Compiled by Y. Shi. ARM Data Center. Data set accessed 2022-11-07 at http://dx.doi.org/10.5439/1507725.

Shupe, MD, Rex, M, Blomquist, B, Persson, POG, Schmale, J, Uttal, T, Althausen, D, Angot, H, Archer, S, Bariteau, L, Beck, I, Bilberry, J, Bucci, S, Buck, C, Boyer, M, Brasseur, Z, Brooks, IM, Calmer, R, Cassano, J, Castro, V, Chu, D, Costa, D, Cox, CJ, Creamean, J, Crewell, S, Dahlke, S, Damm, E, de Boer, G, Deckelmann, H, Dethloff, K, Dütsch, M, Ebell, K, Ehrlich, A, Ellis, J, Engelmann, R, Fong, AA, Frey, MM, Gallagher, MR, Ganzeveld, L, Gradinger, R, Graeser, J, Greenamyer, V, Griesche, H, Griffiths, S, Hamilton, J, Heinemann, G, Helmig, D, Herber, A, Heuzé, C, Hofer, J, Houchens, T, Howard, D, Inoue, J, Jacobi, HW, Jaiser, R, Jokinen, T, Jourdan, O, Jozef, G, King, W, Kirchgaessner, A, Klingebiel, M, Krassovski, M, Krumpen, T, Lampert, A, Landing, W, Laurila, T, Lawrence, D, Lonardi, M, Loose, B, Lüpkes, C, Maahn, M, Macke, A, Maslowski, W, Marsay, C, Maturilli, M, Mech, M, Morris, S, Moser, M, Nicolaus, M, Ortega, P, Osborn, J, Pätzold, F, Perovich, DK, Petäjä, T, Pilz, C, Pirazzini, R, Posman, K, Powers, H, Pratt, KA, Preußer, A, Quéléver, L, Radenz, M, Rabe, B, Rinke, A, Sachs, T, Schulz, A, Siebert, H, Silva, T, Solomon, A, Sommerfeld, A, Spreen, G, Stephens, M, Stohl, A, Svensson, G, Uin, J, Viegas, J, Voigt, C, von der Gathen, P, Wehner, B, Welker, JM, Wendisch, M, Werner, M, Xie, Z, Yue, F. 2022a. Overview of the MOSAiC expedition: Atmosphere. *Elementa: Science of the Anthropocene* **10**(1). ISSN 2325-1026. doi:10.1525/elementa.2021.00060.

Shupe, MD, Rex, M, Blomquist, B, Persson, POG, Schmale, J, Uttal, T, Althausen, D, Angot, H, Archer, S, Bariteau, L, Beck, I, Bilberry, J, Bucci, S, Buck, C, Boyer, M, Brasseur, Z, Brooks, IM, Calmer, R, Cassano, J, Castro, V, Chu, D, Costa, D, Cox, CJ, Creamean, J, Crewell, S, Dahlke, S, Damm, E, de Boer, G, Deckelmann, H, Dethloff, K, Dütsch, M, Ebell, K, Ehrlich, A, Ellis, J, Engelmann, R, Fong, AA, Frey, MM, Gallagher, MR, Ganzeveld, L, Gradinger, R, Graeser, J, Greenamyer, V, Griesche, H, Griffiths, S, Hamilton, J, Heinemann, G, Helmig, D, Herber, A, Heuzé, C, Hofer, J, Houchens, T, Howard, D, Inoue, J, Jacobi, HW, Jaiser, R, Jokinen, T, Jourdan, O, Jozef, G, King, W, Kirchgaessner, A, Klingebiel, M, Krassovski, M, Krumpen, T, Lampert, A, Landing, W, Laurila, T, Lawrence, D, Lonardi, M, Loose, B, Lüpkes, C, Maahn, M, Macke, A, Maslowski, W, Marsay, C, Maturilli, M, Mech, M, Morris, S, Moser, M, Nicolaus, M, Ortega, P, Osborn, J, Pätzold, F, Perovich, DK, Petäjä, T, Pilz, C, Pirazzini, R, Posman, K, Powers, H, Pratt, KA, Preußer, A, Quéléver, L, Radenz, M, Rabe, B, Rinke, A, Sachs, T, Schulz, A, Siebert, H, Silva, T, Solomon, A, Sommerfeld, A, Spreen, G, Stephens, M, Stohl, A, Svensson, G, Uin, J, Viegas, J, Voigt, C, von der Gathen, P, Wehner, B, Welker, JM, Wendisch, M, Werner, M, Xie, Z, Yue, F. 2022b. Overview of the MOSAiC expedition: Atmosphere. *Elementa: Science of the Anthropocene* **10**(1). doi:10.1525/elementa.2021.00060.

Smith, DM. 1996. Extraction of winter total sea-ice concentration in the Greenland and Barents Seas from SSM/I data. *International Journal of Remote Sensing* **17**(13): 2625–2646. doi:10.1080/01431169608949096.

Spreen, G, Kaleschke, L, Heygster, G. 2008. Sea ice remote sensing using AMSR-E 89-GHz channels. *J Geophys Res* **113**: C02S03. doi:10.1029/2005JC003384.

Spreen, G, Kern, S. 2017. Chap. 9, in *Methods of satellite remote sensing of sea ice*. John Wiley & Sons, Ltd: pp. 239–260. doi:https://doi.org/10.1002/9781118778371.ch9.

Stroeve, J, Nandan, V, Willatt, R, Dadic, R, Rostosky, P, Gallagher, M, Mallett, R, Barrett, A, Hendricks, S, Tonboe, R, McCrystall, M, Serreze, M, Thielke, L, Spreen, G, Newman, T, Yackel, J, Ricker, R, Tsamados, M, Macfarlane, A, Hannula, HR, Schneebeli, M. 2022. Rain on snow (ROS) understudied in sea ice remote sensing: a multi-sensor analysis of ROS during MOSAiC (Multidisciplinary drifting Observatory for the Study of Arctic Climate). *The Cryosphere* **16**(10): 4223–4250. doi:10.5194/tc-16-4223-2022. `https://tc.copernicus.org/articles/16/4223/2022/`.

Svendsen, H, Mätzler, C, Grenfell, TC. 1987. A model for retrieving total sea ice concentration from a spaceborne dual-polarized passive microwave instrument operating near 90 GHz. *International Journal of Remote Sensing* **8**(10): 1479–1487. ISSN 0143-1161. doi:10.1080/01431168708954790.

Thielke, L, Huntemann, M, Spreen, G. 2022. Lead classification maps from helicopter-borne surface temperatures during the MOSAiC expedition. PANGAEA. doi:10.1594/PANGAEA.951569. `https://doi.org/10.1594/PANGAEA.951569`.

Tjernström, M, Shupe, MD, Brooks, IM, Persson, POG, Prytherch, J, Salisbury, DJ, Sedlar, J, Achtert, P, Brooks, BJ, Johnston, PE, Sotiropoulou, G, Wolfe, D. 2015. Warm-air advection, air mass transformation and fog causes rapid ice melt. *Geophysical Research Letters* **42**(13): 5594–5602. doi:https://doi.org/10.1002/2015GL064373.

Tonboe, R, Andersen, S, Toudal, L, Heygster, G. 2006. Sea ice emission modelling applications, in Mätzler, C, ed., *Thermal Microwave Radiation - Applications for Remote Sensing*, *IET Electromagnetic Wave Series*, vol. 52. The Institution of Engineering and Technology (IET): pp. 382–400. (IET Electromagnetic Wave Series, vol. 52). Section: 4.16.

Tonboe, RT, Andersen, S, Toudal, L. 2003. Anomalous winter sea ice backscatter and brightness temperatures. Danish Meteorological Institute, Copenhagen. Scientific Report 03-13.

Troitsky, AV, Osharin, AM, Korolev, AV, Strapp, JW. 2003. Polarization of Thermal Microwave Atmospheric Radiation Due to Scattering by Ice Particles in Clouds. *Journal of the Atmospheric Sciences* **60**(13): 1608 – 1620. doi:10.1175/1520-0469(2003)60<1608:POTMAR>2.0.CO;2.

Ulaby, FT, Long, DG, Blackwell, WJ, Elachi, C, Fung, AK, Ruf, CS, Sarabandi, K, Zebker, HA, van Zyl, JJ. 2013. Microwave Radar and Radiometric Remote Sensing.

Valkonen, E, Cassano, J, Cassano, E. 2021. Arctic Cyclones and Their Interactions With the Declining Sea Ice: A Recent Climatology. *Journal of Geophysical Research: Atmospheres* **126**(12): e2020JD034366. ISSN 2169-8996. doi:10.1029/2020JD034366.

Wagner, DN, Shupe, MD, Cox, C, Persson, OG, Uttal, T, Frey, MM, Kirchgaessner, A, Schneebeli, M, Jaggi, M, Macfarlane, AR, Itkin, P, Arndt, S, Hendricks, S, Krampe, D, Nicolaus, M, Ricker, R, Regnery, J, Kolabutin, N, Shimanshuck, E, Oggier, M, Raphael, I, Stroeve, J, Lehning, M. 2022. Snowfall and snow accumulation during the MOSAiC winter and spring seasons. *The Cryosphere* **16**(6): 2373–2402. doi:10.5194/tc-16-2373-2022. https://tc.copernicus.org/articles/16/2373/2022/.

Walbröl, A, Crewell, S, Engelmann, R, Orlandi, E, Griesche, H, Radenz, M, Hofer, J, Althausen, D, Maturilli, M, Ebell, K. 2022. Atmospheric temperature, water vapour and liquid water path from two microwave radiometers during MOSAiC. *Scientific Data* **9**(1): 534. doi:10.1038/s41597-022-01504-1.

Wendisch, M, Brückner, M, Burrows, JP, Crewell, S, Dethloff, K, Ebell, K, Lüpkes, C, Macke, A, Notholt, J, Quaas, J, Rinke, A, Tegen, I. 2017. Understanding causes and effects of rapid warming in the Arctic. *Eos* **98**(8): 22–26. doi:10.1029/2017EO064803.

Wendisch, M, Brückner, M, Crewell, S, Ehrlich, A, Notholt, J, Lüpkes, C, Macke, A, Burrows, JP, Rinke, A, Quaas, J, Maturilli, M, Schemann, V, Shupe, MD, Akansu, EF, Barrientos-Velasco, C, Bärfuss, K, Blechschmidt, AM, Block, K, Bougoudis, I, Bozem, H, Böckmann, C, Bracher, A, Bresson, H, Bretschneider, L, Buschmann, M, Chechin, DG, Chylik, J, Dahlke, S, Deneke, H, Dethloff, K, Donth, T, Dorn, W, Dupuy, R, Ebell, K, Egerer, U, Engelmann, R, Eppers, O, Gerdes, R, Gierens, R, Gorodetskaya, IV, Gottschalk, M, Griesche, H, Gryanik, VM, Handorf, D, Harm-Altstädter, B, Hartmann, J, Hartmann, M, Heinold, B, Herber, A, Herrmann, H, Heygster, G, Höschel, I, Hofmann, Z, Hölemann, J, Hünerbein, A, Jafariserajehlou, S, Jäkel, E, Jacobi, C, Janout, M, Jansen, F, Jourdan, O, Jurányi, Z, Kalesse-Los, H, Kanzow, T, Käthner, R, Kliesch, LL, Klingebiel, M, Knudsen, EM, Kovács, T, Körtke, W, Krampe, D, Kretzschmar, J, Kreyling, D, Kulla, B, Kunkel, D, Lampert, A, Lauer, M, Lelli, L, von Lerber, A, Linke, O, Löhnert, U, Lonardi, M, Losa, SN, Losch, M, Maahn, M, Mech, M, Mei, L, Mertes, S, Metzner, E, Mewes, D, Michaelis, J, Mioche, G, Moser, M, Nakoudi, K, Neggers, R, Neuber, R, Nomokonova, T, Oelker, J, Papakonstantinou-Presvelou, I, Pätzold, F, Pefanis, V, Pohl, C, van Pinxteren, M, Radovan, A, Rhein, M, Rex, M, Richter, A, Risse, N, Ritter, C, Rostosky, P, Rozanov, VV, Donoso, ER, Garfias, PS, Salzmann, M, Schacht, J, Schäfer, M, Schneider, J, Schnierstein, N, Seifert, P, Seo, S, Siebert, H, Soppa, MA, Spreen, G, Stachlewska, IS, Stapf, J, Stratmann, F, Tegen, I, Viceto, C, Voigt, C, Vountas, M, Walbröl, A, Walter, M, Wehner, B, Wex, H, Willmes, S, Zanatta, M, Zeppenfeld, S. 2023. Atmospheric and Surface Processes, and Feedback Mechanisms Determining Arctic Amplification: A Review of First Results and Prospects of the (AC)3 Project. *Bulletin of the American Meteorological Society* **104**(1): E208 – E242. doi:https://doi.org/10.1175/BAMS-D-21-0218.1. https://journals.ametsoc.org/view/journals/bams/104/1/BAMS-D-21-0218.1.xml.

Wever, N, Rossmann, L, Maaß, N, Leonard, KC, Kaleschke, L, Nicolaus, M, Lehning, M. 2019. Version 1 of a sea ice module for the physics based, detailed, multi-layer SNOWPACK model. *Geosci Model Dev Discuss* **2019**: 1–30. doi:https://doi.org/10.5194/gmd-2019-97.

Woods, C, Caballero, R. 2016. The Role of Moist Intrusions in Winter Arctic Warming and Sea Ice Decline. *J Clim* **29**(12): 4473–4485. ISSN 0894-8755. doi:10.1175/JCLI-D-15-0773.1.

Woods, C, Caballero, R, Svensson, G. 2013. Large-scale circulation associated with moisture intrusions into the Arctic during winter. *Geophysical Research Letters* **40**(17): 4717–4721. doi:https://doi.org/10.1002/grl.50912.

Zhang, P, Chen, G, Ting, M, Ruby Leung, L, Guan, B, Li, L. 2023. More frequent atmospheric rivers slow the seasonal recovery of Arctic sea ice. *Nature Climate Change* pp. 1–8. ISSN 1758-6798. doi:10.1038/s41558-023-01599-3. https://www.nature.com/articles/s41558-023-01599-3.

Contributions

Janna E. Rückert and Philip Rostosky contributed equally to this work. First description and interpretation of event: LK. Conception and design of this study: JR, PR, MH, GS. Acquisition of data: MH, GS, LK, AM, RN, JS. Analysis and interpretation of data: JR, PR, MH, DCS, KE, LK, JL, AM, AW, GS. Drafting, and revising this article: All authors.

Approval of the version to be submitted: All authors.

Acknowledgements

This work was carried out, and data used in this manuscript was produced, as part of the international Multidisciplinary drifting Observatory for the Study of the Arctic Climate (MOSAiC) with the tag MOSAiC20192020. We thank all persons involved in the expedition of the research vessel *Polarstern* during MOSAiC in 2019–2020 (AWI_PS122_00) as listed in Nixdorf et al. (2021). Additionally we would like to thank Robert Hausen and Linda Thielke for information and discussions, Matthew Shupe for support with the meteorological tower measurements, Ronny Engelmann and the TROPOS institute for acquiring the HATPRO measurements onboard, Tânia Casal, Craig Donlon from ESA, and Roger Jové Casulleras from Balamis for supporting HUTRAD for MOSAiC, and Eric Brossier and Calle Schönning for their assistance with TLS measurements.

Funding information

We gratefully acknowledge the funding by the Deutsche Forschungsgemeinschaft (DFG, German Research Foundation) through the Transregional Collaborative Research Centre TRR-172 “ArctiC Amplification: Climate Relevant Atmospheric and SurfaCe Processes, and Feedback Mechanisms $(AC)^3$” (grant 268020496) and the MOSAiCmicrowaveRS project (grant 420499875). Further funding was provided by the Bundesministerium für Bildung und Forschung (BMBF) through the IceSense project (grant BMBF 03F0866B). The microwave radiometer HUTRAD measurements were funded by ESA through the CIMRex (contract 4000125503/18/NL/FF/gp) project; the HATPRO radiometer by BMBF under FKZ: 01LKL1603A. D.C.S. was supported by NSF OPP-1724540.

Competing interests

The authors have declared that no competing interests exist.

6. Supplemental material

6.1. S1 - MEMLS_ice initialization

MEMLS_ice is a microwave emission model for layered snow and ice to simulate the upwelling brightness temperatures of a snow-ice system in the microwave regime, based on its dielectric properties. The model needs several snow and ice properties as input data. For the snow, most of these properties like density, exponential correlation length or temperature can be obtained from SnowMicroPen and snow pit samples, while some parameters like snow wetness or interface roughness have to be assumed. The roughness is modelled by the modification of the interface reflectivity following Choudhury et al. (1979). In principle, a glazing layer can lead to coherent reflections in the microwave regime. However, as we have not enough information about the thickness and uniformity of that ice layer, we do not calculate coherent reflections in our modelling of the glazed layer. Note that coherence is in principle implemented in MEMLS but deactivated for our purposes. During the warm air intrusion events, one ice core sample was taken at April 17 in the vicinity (i.e., $\mathcal{O}100\,$m) of the remote sensing site. We use this ice core as first guess for the sea ice properties and then slightly varied the salinity and density profiles to obtain brightness temperatures at 6.9 GHz that are similar to the ground-based radiometer observations before the warm air intrusion. For all layers, the deviations from the ice core samples are less than 1 ppt for salinity and less than 50 $\mathrm{Kgm^{-3}}$ for the density. Also note that the Central Observatory was on second-year ice (with a low amount of salinity in the upper layers) at the beginning of the expedition in 2019 but that there was new ice formation during the winter. On the satellite footprint scale a mixture of second- (dominating) and first-year ice prevailed. Except for the ice temperature, for which a linear fit is used between the snow/ice and ice/ocean interface temperatures, the ice profile properties are kept constant for the whole time series. Since the warm air intrusions were short-term events and the temperature at the snow-ice interface only slightly changed, this is a valid assumption. Table S1 shows the initialization profile for April 08 07:40 based on the SMP profile S49M2235 (Macfarlane et al., 2021) for 6.9 GHz. At the microwaves frequencies investigated here, only the upper ice layer is relevant due to the high absorption in the ice. Therefore, only the upper 40 cm of the ice are shown (bottom five rows in Table S1). The model was initialized with 2 m thick ice. Thus there is no influence from the ocean below. The downwelling sky temperature is calculated with the radiative transfer model PAMTRA (Mech et al., 2020) using the HATPRO TWV and LWP data as well as profiles from radiosondes launched during MOSAiC.

Note that the snow height from the SMP profiles was usually lower than the snow in the field of view of the radiometers due to enhanced snow accumulation. The TLS scan data provides accurate relative differences of snow height. In order to obtain absolute values, we use the measurement of the maximum snow dune height with a ruler stick on April 22, namely 90 cm as reference point. The acquired snow depths are in agreement with other manual ruler stick measurements of snow height performed close to the radiometer footprints. Table S2 shows the snow height at the different sensors from TLS scans from April 17 and April 22. Figure S1 shows the surface elevation at April 22 based on a TLS scan. In addition, the FoV of the different frequencies of the ground-based radiometers is shown. High snow dunes were forming during the second warm air intrusion in front of the radiometers.

6.2. S2 - SMP-based modelling

Figure S2 shows the simulated brightness temperatures at different frequencies for the time period before the warming events (April 08 to April 15, blue) and after the warming events (April 21 - April 27, red). For the simulations, the SMP profiles were averaged to layers of at least 2 cm thickness. To maintain the layering

Table S1: Initialization profile for the MEMLS_ice simulation for April 08 07:40 for 6.9 GHz. Shown are the parameters: layer thickness LT (cm), Temperature T (K), Density ρ (Kgm^{-3}), exponential correlation length pc (mm), wetness W, salinity S (ppt), interface roughness R (mm). Parameters used for fitting the simulations are shown in *italics*. The downwelling sky temperature at 6.9 GHz is 6.1 K

Depth	LT	T	ρ	pc	W	S	R
0	2.1	250.1	269.8	0.292	0	0	0
2.1	3.3	250.9	374.6	0.344	0	0	0
5.4	4.0	251.9	311.5	0.298	0	0	0
9.4	2.8	252.5	299.0	0.271	0	0	0
12.2	2.0	252.8	287.7	0.271	0	0	0
14.2	3.0	253.0	287.7	0.271	0	0	0
17.2	2.1	252.9	312.8	0.299	0	0	0
19.3	3.0	252.8	264.6	0.203	0	0	0
22.3	8	253.0	*880*	*0.450*	0	*3.08*	*2.20*
30.3	8	253.5	*880*	*0.450*	0	*2.93*	0
38.3	8	253.2	*880*	*0.450*	0	*2.80*	0
46.3	8	253.4	*880*	*0.450*	0	*2.66*	0
54.3	8	253.6	*880*	*0.450*	0	*2.50*	0

Table S2: Average snow height (cm) in the FoV of the different channels (GHz) at April 17 and April 22

Date	6.9	10.7	19	89
April 17	48	46	45	44
April 22	48	53	46	71

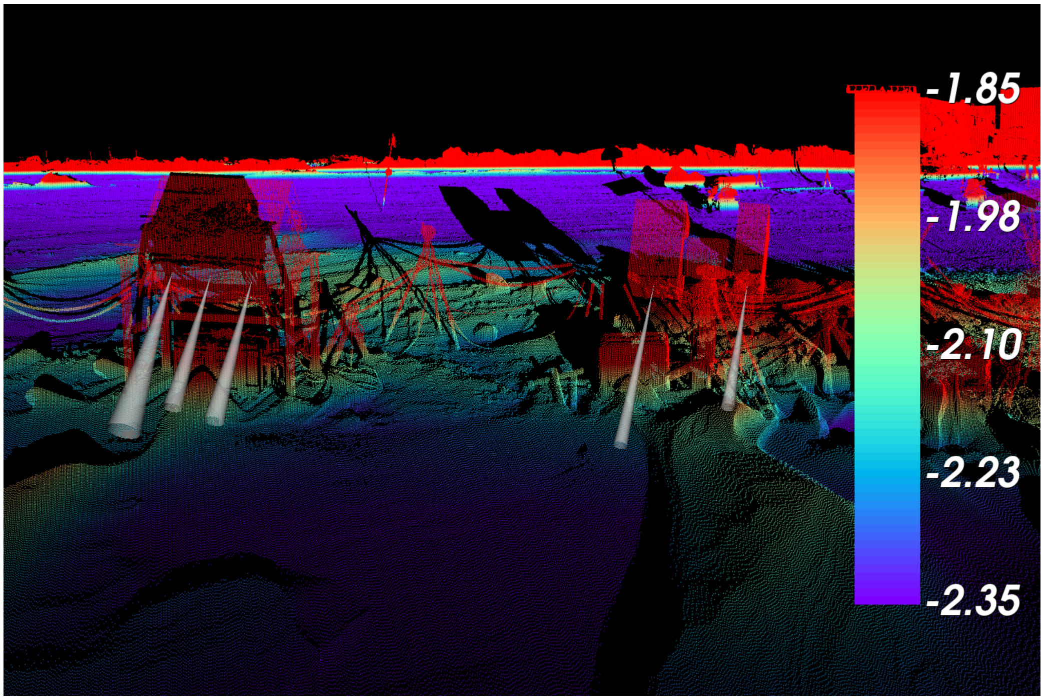

Figure S1: TLS surface height with respect to the height of the laser scanner (2.5 m) from 22 April. The cones indicate the viewing direction if the different sensors. From left to right: HUTRAD frequencies (GHz): 10.7, 18.7 (not used), 6.9, SBR frequencies (GHz): 19, 89.

in the snowpack, snow type classifications provided by Kaltenborn et al. (2022) were used for the initial step. Strong changes in simulated brightness temperatures are visible at all frequencies. At 6.9 GHz and 19 GHz, brightness temperatures are higher after the warming events caused by a generally higher snowpack temperature. In contrast, at 37 GHz, increased scattering due to snow metamorphism leads to a decrease of brightness temperatures. Note that no glazed layer was used in these simulations.

6.3. S3 - Glazed layer observations

Figure S3 shows the TLS reflectance for April 17 and April 22. Glazed areas have low TLS reflectance (dark purple colors) in the near-IR due to increased absorption and specular reflections. On April 17, only a few patchy glazed areas are

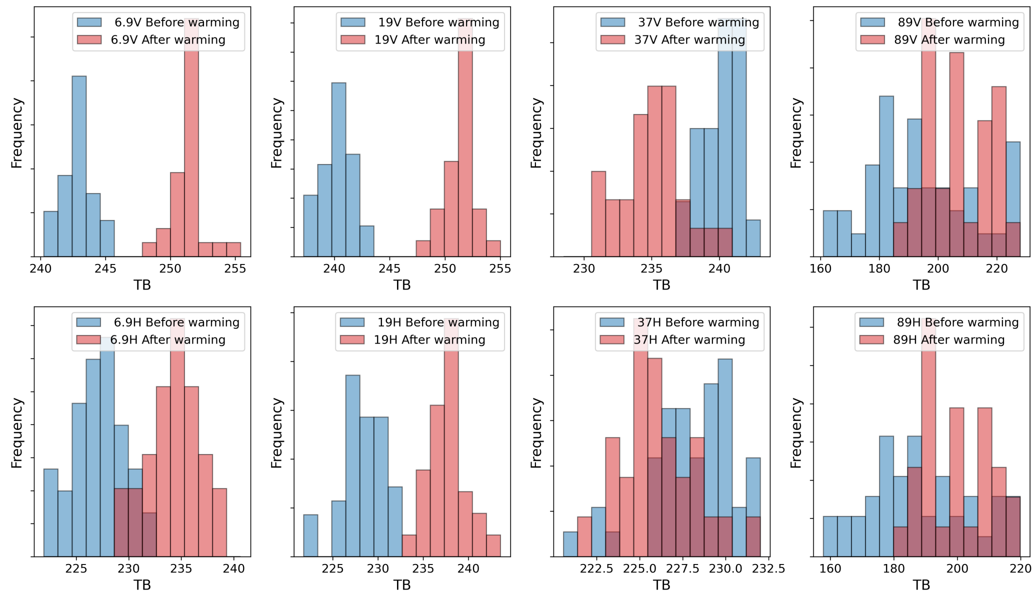

Figure S2: Simulated brightness temperature from SMP profiles. The data is split into the periods from April 08 - April 15 (blue) and April 21 - April 27 (red).

present (e. g., the dark purple patch in the upper right) and none are within the instruments' footprints. On April 22, widespread glazing was observed on unaltered snow surfaces (e. g., upper portion of figure). However, the snow drifts that formed in the instruments' footprints were not glazed. The glazing was also evident from visual observations. Figure S4 shows the glazed snow surfaces observed on April 22 at the remote sensing site (Figure S4, left). The snow in front of the radiometers is freshly accumulated. Also on the panorama camera mounted on *Polarstern*, the glazing was visible at April 22 (Figure S4, right).

6.4. S4 - Ground-based radiometer observations

We focus on two microwave radiometers deployed during MOSAiC observing the surface at frequencies ranging from 6.9 GHz to 89 GHz, similar to AMSR2. Details are provided in Table S3. They were installed next to each other on the ice facing the same area but the footprints do not overlap (see Figure S1). The low-frequency system of HUTRAD (Helsinki University of Technology Radiometer) (Hallikainen et al., 1996; Colliander et al., 2007; Lemmetyinen et al., 2009) measures at three frequencies at 6.825, 10.65 and 18.7 GHz, at two orthogonal

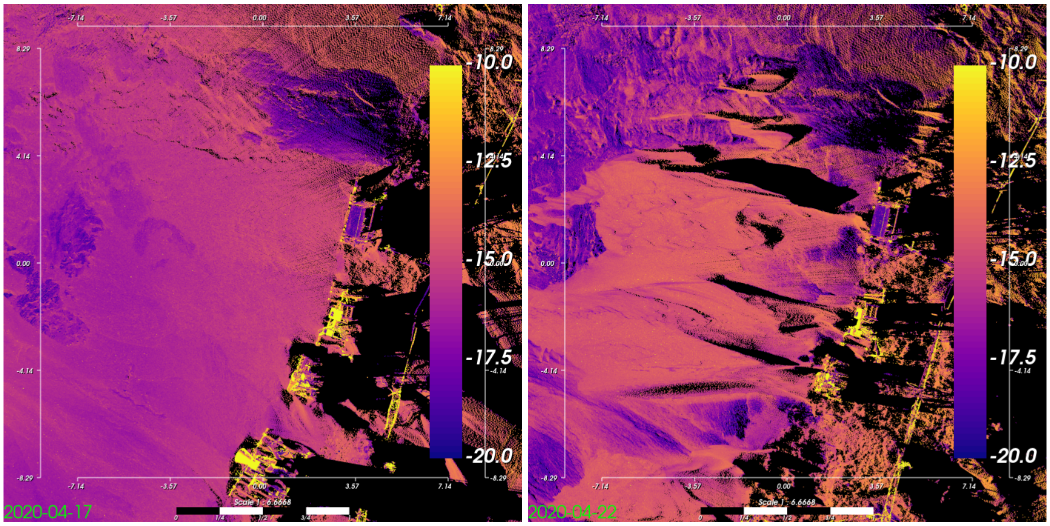

Figure S3: Glazed snow surfaces observed in Terrestrial Laser Scanning (TLS) reflectance near the HUTRAD and SBR instruments on April 17 (left) and April 22 (right). Scale bars are in meters.

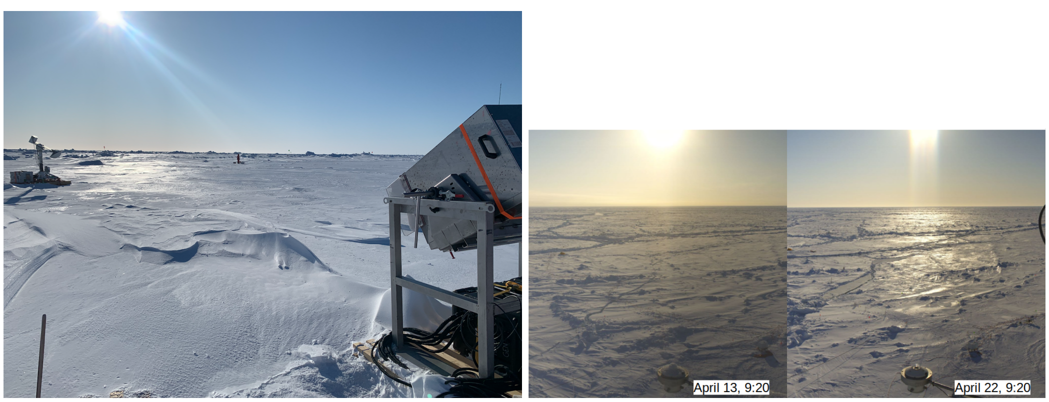

Figure S4: Left: Image from April 22 at the remote sensing site (photo: Lars Kaleschke). Right: panorama image from Panomax webcam onboard *Polarstern* (`https://www.mosaic-panorama.org/`) from April 13 and April 22.

polarizations H and V. During MOSAiC, HUTRAD had a sampling rate of 1 s, the dataset used here was averaged to 1 minute temporal resolution in order to decrease fluctuations. HUTRAD was observing at a fixed incident angle of 45°. With an instrument height of 0.8 m the largest footprint size (at vertically-polarized 6.9 GHz) is 30 cm × 42 cm. The radiometer was deployed at a fixed location during the whole period investigated. The uncertainty (i.e., 2× standard deviation) of the calibrated brightness temperature is estimated around 3 K. It is to note that the internal temperature control of the 18.7 GHz receiver failed early on in the MOSAiC campaign, which made measurements unstable and unusable for our investigation.

The surfaced based radiometer from University of Manitoba (SBR) radiometer observes at 19, 37 and 89 GHz (Radiometrics, 2004). Radiometric properties are provided in Table S3, for more detailed specifications see Table 1 in Derksen et al. (2012). The SBR was measuring in scanning-mode with incident angle varying from 40° to 70° in 5° steps. The sampling rate varies between 1 s and 5 s. For this study, we only use the measurements at 55°, since most data was collected at this angle. The footprint size is about 20 cm × 35 cm (assuming 1.1 m instrument height). Similar to HUTRAD the SBR data is resampled to 1 minute temporal resolution. The uncertainty of the observations at 89 GHz is similar to the lower frequencies (6 K for horizontally- and 5 K for vertically-polarized TB). Unfortunately, during leg 3, the 37 GHz receiver was not functioning.

As the 18.7 GHz horizontally-polarized channel from HUTRAD was unstable during our period of interest, we show the values measured by SBR which measures at 19 GHz. During the first warming event some values from SBR (between two calibrations) had to be removed because they show unrealistic fluctuations.

Corrupted scans and data points with clearly non-physical values were filtered out manually for Figure 9.

Figure S1 illustrates the formation of snow dunes in front of the radiometers that further increase the local (intra- and inter-footprint) variability of the snow conditions.

Data accessibility statement

The AMSR2 satellite data is available via Japan Aerospace Exploration Agency's G-Portal `https://gportal.jaxa.jp/gpr/?lang=en`. The NOAA/NSIDC Climate Data Record of Passive Microwave Sea Ice Concentration, Version 4 is available via `https://nsidc.org/data/g02202/versions/4`. The OSI-430-b SIC product data is available via `https://`

Table S3: HUTRAD and SBR radiometric properties: Shown are frequency (GHz), polarization P, radiometric bandwidth BW (MHz) and sensitivity (K), incidence angle θ (degree), field of view FoV given by the half power beam width (degree) and the FoV on the ground (cm) based on an instrument height of 0.8 m (HUTRAD) and 1.1 m (SBR).

	HUTRAD				SBR	
Frequency (GHz)	6.9		10.7		19	89
Polarization	H	V	H	V	H/V	H/V
Bandwidth (MHz)	310	310	120	120	1000	4000
Sensitivity (K)	0.09	0.11	0.24	0.22	0.04	0.08
θ (°)	45	45	45	45	55	55
Field of View (°)	11.2	14.8	6.6	9.1	6	5.88
Field of View (cm)	22 × 32	30 × 42	13 × 19	18 × 26	20 × 35	20 × 35

`osi-saf.eumetsat.int/` (copyright 2021 EUMETSAT). The radiometer, snow, temperature, laser scan and radiosonde data used in this manuscript was produced as part of the international Multidisciplinary drifting Observatory for the Study of the Arctic Climate (MOSAiC) with the tag MOSAiC20192020 and the Project ID: AWI PS122 00. The HUTRAD radiometer data is available via PANGAEA `https://doi.org/10.1594/PANGAEA.954608`. The radiosonde data is available via PANGAEA `https://doi.org/10.1594/PANGAEA.928656`. The HATPRO LWP data product is available via PANGAEA `https://doi.org/10.1594/PANGAEA.941389`. The near-surface temperature measurements are available from the Arctic Data Center (Cox et al., 2021). The Present Weather Detector 22 precipitation gauge data is accessible via ARM: `https://adc.arm.gov/discovery/#/results/instrument_code::pwd`, last access: 07 November 2022. The SBR radiometer is available via PANGAEA `https://doi.pangaea.de/10.1594/PANGAEA.956108` (dataset in review). The TLS data is available via the Arctic Data Center (Clemens-Sewall, 2021). ERA5 data are made available by the Copernicus Climate Change Service (C3S) at `https://cds.climate.copernicus.eu/cdsapp#!/home`. C3S (2017): ERA5. Fifth generation of European Centre for Medium-range Weather Forecasts atmospheric reanalyses of the global climate. Copernicus Climate Change Service Climate Data Store, 2017–2020.